2007

Evanescent Microwave Characterization of carbon Nanotube Films Grown on Silicon Carbide Substrate

Kineshma Munbodh
Wright State University

EVANESCENT MICROWAVE CHARACTERIZATION OF CARBON NANOTUBE FILMS GROWN ON SILICON CARBIDE SUBSTRATE

A thesis submitted in partial fulfillment
of the requirements for the degree of
Master of Science

By

KINESHMA MUNBODH

B.S., University of Mauritius, 2005

Wright State University, 2007

WRIGHT STATE UNIVERSITY

SCHOOL OF GRADUATE STUDIES

June 7, 2007

I HEREBY RECOMMEND THAT THE THESIS PREPARED UNDER MY SUPERVISION BY Kineshma Munbodh ENTITLED Evanescent microwave characterization of carbon nanotube films grown on silicon carbide substrate BE ACCEPTED IN PARTIAL FULFILLEMENT OF THE REQUIREMENT FOR THE DEGREE OF Master of Science.

Gregory Kozlowski, Ph.D
Thesis advisor

Lok Lew Yan Voon, Ph.D
Department chair

Committee on
Final Examination

Gregory Kozlowski, Ph.D

Lok Lew yan Voon, Ph.D

John Boeckl, Ph.D

Joseph F. Thomas, Jr., Ph.D.
Dean, School of Graduate Studies.

Munbodh, Kineshma., M.S., Department of Physics, Wright State University, 2007.

Evanescent Microwave Characterization of carbon Nanotube Films Grown on Silicon Carbide Substrate.

ABSTRACT

The electromagnetic characterization of carbon nanotube films (CNT) grown by the surface decomposition of silicon carbide (SiC) has been performed. The CNT films formed on the carbon and silicon terminated face of the SiC substrate were uncapped by an annealing process at a temperature of 400^0 C with dwelling time up to 60 minutes in oxygen or carbon dioxide atmosphere. X-Y scans of the quality factor were used to deduce the local conductive properties of the films measured by evanescent microwave microscopy. Real and imaginary permittivity values, as determined by these electromagnetic measurements, provided valuable information for future field emission testing on these films. A theoretical model, adapted from the literature, was used to find the real and imaginary component of the permittivity of the CNT films. The results showed improvement in the surface conductivity of the samples after the annealing treatment.

TABLE OF CONTENTS

LIST OF FIGURES

LIST OF TABLES

ACKNOWLEGEMENTS

My foremost thanks go to my thesis advisor, Prof. G. Kozlowski for his help, guidance, invaluable suggestions and advice at all times during this research. He has been very patient and helped me tremendously in the writing of the thesis.

I would like to extend my sincere thanks to Dr. R. Kleismit for tremendous help in the acquiring of the evanescent microwave data and providing invaluable insight into the function of the equipment and the interpretation of the data.

I am grateful to Dr J. Boeckl for providing the carbon nanotube samples and his explanation in understanding the subject.

My sincerest gratitude goes to Prof. L. Lew Yan Voon for all of his care and support over the past two years. He has given me the opportunity to join Wright State University and has been there for me since the very beginning. Prof. Lok has made my time here at Wright State University very enjoyable.

Special thanks to all my classmates for their help and support during the two years at Wright State University.

A heart-felt thanks to my parents for their unwavering support and encouragement in my studies throughout my school years.

GOAL OF THESIS

The goal of my thesis is to study the electromagnetic properties of carbon nanotube films grown on silicon carbide substrates using evanescent microwave microscopy. These films were subjected to an annealing treatment in order to improve their local conductive properties, a useful benefit for field-emission application. X-Y scans of the Q-factor were carried out to see local changes of conductivity on the surface of these films. Structural and chemical characterization were performed to see any changes which took place after the annealing process. The method of images was used as a theoretical model to interpret evanescent microwave microscopy measurements and to find the real and imaginary permittivity parameters of treated and untreated CNT films.

This project has been a collaborative work between the Air Force Research Laboratory (AFRL) and Wright State University. The CNT samples were grown by the catalyst-free method at Wright Patterson Air Force Base because of the equipment availability and their expertise in this area. The samples were annealed and the electromagnetic characterization was carried out at Wright State University. A Theoretical model, adapted from the literature, will be used to determine the complex permittivity parameters of the treated and untreated CNT films. The equations from this model will be used to derive and calculate the frequency shifts and reciprocal of the quality factor when the probe-tip touches the sample. The chemical and structural characterization of the samples were important in order to have a better insight into the changes taking place after annealing, and were done at the Base, due to the unavailability of the equipment on-campus.

Chapter 1 presents a brief introduction to the synthesis methods of carbon nanotubes, their physical properties and potential applications.

Chapter 2 describes the Fowler-Nordheim theory of field emission, which relates the emission current to the local field and the work function. A summary of the current knowledge of the field emission of CNT grown by the surface decomposition of silicon carbide is also given.

Chapter 3 the describes the evanescent microwave microscopy set-up and, based on the method of images, a theoretical model of frequency shift for the microwave resonator due to material perturbation.

Chapter 4 gives a complete description of the preparation of the CNT samples, which were grown at Wright Patterson Air Force Base. The complete annealing treatment, performed in our laboratory, will also be described.

Chapter 5 describes the growth mechanism of the CNT films and their structural and chemical characterization.

In chapter 6, evanescent microwave data for treated and untreated CNT films are given. The theoretical model, adapted from the literature and described in chapter 3, is derived here to find the frequency and reciprocal of the Q-factor shifts for the case when the probe tip of the microscope touches the film.

In chapter 7, the interpretation of our experimental data provided by SEM, TEM, AFM, XRD, EDS and evanescent microwave microscopy is included. In particular, important X-Y scans of Q-factor for treated and untreated CNT films are presented. Theoretical values of real and imaginary components of permittivity of these films are given.

Chapter 8 provides a summary of important findings in my thesis and some suggestions for future work.

CHAPTER 1

INTRODUCTION

1.1 Synthesis of carbon nanotubes

Carbon nanotubes (CNT) have novel properties that make them excellent candidates for applications in nanoelectronics and computing. The main applications of the CNT are for the production of field emission devices, sensors and nano electromechanical devices (NEMS). Its high electrical conductivity and nanosize tip makes CNT a very good emitter compared to conventional metal emitters. The sharpness of the tip also lowers the voltage at which emission current is obtained. An application that is being exploited is in the making of field-emission displays.

Carbon nanotubes can be grown using a variety of methods, each producing samples of different purity, shape, size and structure (either multi- or single-walled) [1]. The methods, which are commonly used, are:

(1) Arc discharge.

(2) Laser ablation.

(3) Chemical vapor deposition.

(4) Surface decomposition of silicon carbide.

1.1.1 Arc discharge synthesis

In the arc discharge method, a direct current arc operates in a 1 mm wide gap between two graphite electrodes housed in a water cooled chamber as shown in Fig. 1. A low voltage (12-25 V) and high current (12-50 A) is used. An atmosphere comprised of an inert gas, such as helium (He) or argon (Ar), is pumped into the chamber at a pressure range from 100 Torr to 1000 Torr. The anode is consumed in the arc and the CNT grow on the cathode in the presence of a mixture of pure powdered metals, such as iron, nickel and cobalt.

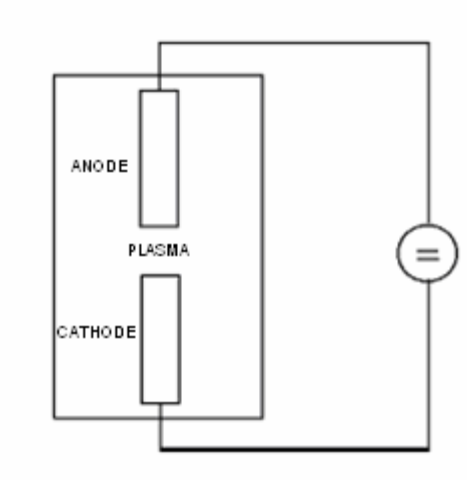

Fig. 1. Schematic of an arc discharge chamber [1].

1.1.2 Laser ablation

In this method, a laser beam interacts with a graphite target in the presence of metal catalysts such as cobalt and nickel as shown in Fig. 2 [2]. Laser pulses enter the tube and hit the target causing the CNT to condense on the collector outside the furnace. The process takes place in the presence of an inert gas flow.

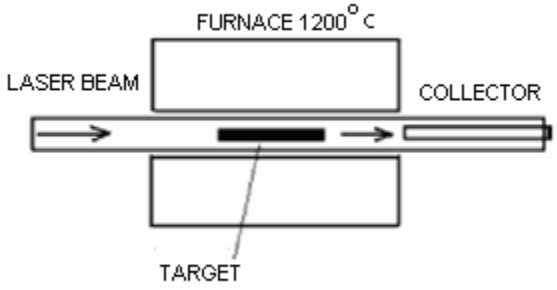

Fig. 2. Laser beam vaporizes target of a mixture of graphite and metal catalysts [1].

1.1.3 Chemical vapor deposition (CVD)

In this method, a hydrocarbon is decomposed in the presence of a transition metal catalyst in a chemical vapor reactor as shown in Fig. 3. A hydrocarbon gas, such as acetylene is usually used as a source of carbon in the temperature range of 500^0 C-800^0 C

to produce multi-walled CNT. A higher temperature, in the range 800^0 C-1200^0 C, is required to grow single-walled CNT.

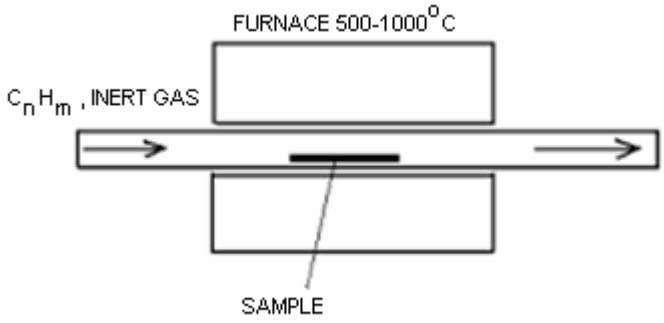

Fig. 3. Hydrocarbon gas is decomposed in a quartz tube in a furnace [1].

1.1.4 Surface decomposition of silicon carbide

The detailed description of this method will be given in Chapter 5.

1.2 Physical properties of carbon nanotubes

Carbon nanotubes have a very simple chemical composition and atomic bonding configuration [3]. They are held together by carbon-carbon bonds which are exceedingly strong mechanically and chemically and are very stable thermally. A single-walled nanotube is formed by rolling a graphene sheet into a cylinder.

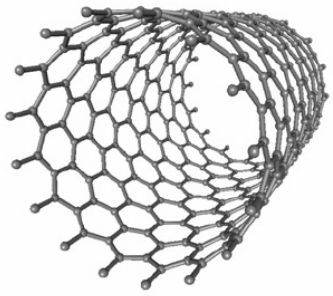

Fig. 4. Single-walled carbon nanotube [4].

Tab.I below summarizes the general properties of CNT [5].

Tab.I. Summary of the general properties of carbon nanotubes.

Property	**Description**
Mechanical	Density of 1.4 g/cm^3 (steel's density is in the range 7.7-8.03 g/cm^3). Tensile strength of 45 GPa (20 times that of steel). Young's Modulus of 1 TPa (5 times that of steel). Strength to weight ratio is 500 times that of steel.
Electrical	Metallic or semiconducting properties depend on the CNT structure. Metallic CNT have electrical current density 1000 times greater than metals such as silver and copper.
Thermal	Thermal conductivity of individual multi-walled CNT is greater than 3000 W/m K which is larger than that of natural diamond and base plane of graphite [6].
Chemical	The strong carbon to carbon bonds make them chemically inert.

The carbon nanotubes can be grown in different configurations described by a so-called chiral vector $\mathbf{c}_h$

$$\mathbf{c}_h = n\,\mathbf{a}_1 + m\,\mathbf{a}_2$$

where n and m are the integers and $\mathbf{a}_1$ and $\mathbf{a}_2$ are the unit vectors in the hexagonal lattice as shown in Fig. 5.

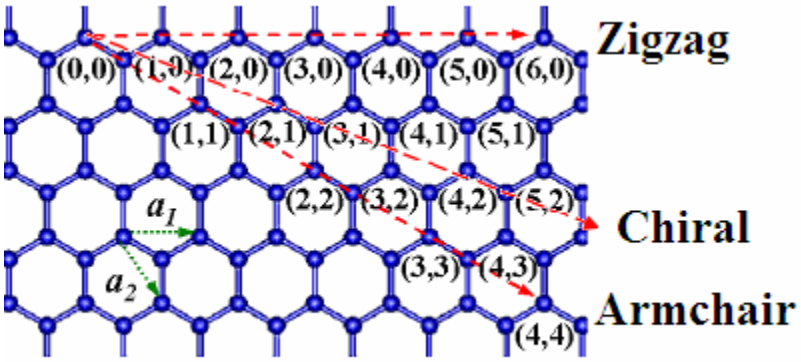

Fig. 5. Schematic diagram of the graphene sheet showing the chiral vector for a zigzag, chiral and armchair carbon nanotube [7].

When the graphene sheet is rolled, the tail and the tip of the chiral vector meet together to form the circumference of the CNT with circular cross-section. The different values of n and m lead to different CNT structures and different diameters D of the tube

$$D = ((3)^{1/2}/\pi)\, a_{c\text{-}c}(n^2 + m^2 + nm)^{1/2}$$

where $a_{c\text{-}c}$ is the distance between neighboring carbon atoms in a flat graphene sheet which is approximately 1.42 Å [1,2].

According to the chiral angle defined as the angle between $\mathbf{c}_h$ and unit vector $\mathbf{a}_1$ and chiral vectors, single-walled CNT is classified as zigzag, armchair and chiral types (Tab.II and Fig. 6) [2].

Tab.II. Geometrical description of CNT.

Type of CNT	Chiral angle (^{0})	Chiral vector (n,m)
Zigzag	0	(n,0)
Armchair	30	(n,n)
Chiral	between 0 and 30	(n,m) for n ≠ m

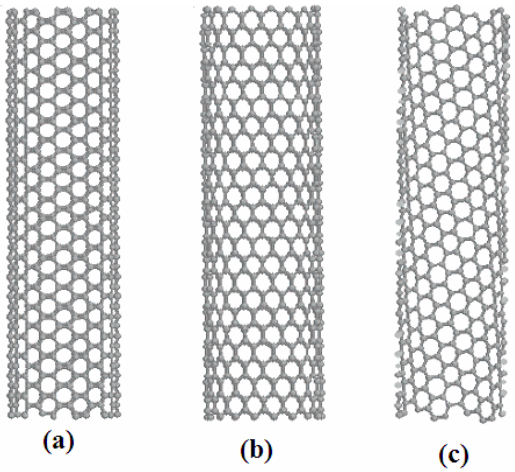

Fig. 6. Armchair (a), zigzag (b) and chiral (c) carbon nanotubes [3].

The (n,m) values dictate the chirality and the diameter of the carbon nanotube, which are the key parameters in determining their electrical properties. The armchair

tubes are conducting, whereas the zigzag and chiral tubes are mostly semiconducting with a band gap between 1 meV and 1 eV [3].

CHAPTER 2

FIELD EMISSION

The derivation of the Fowler-Nordheim equation describing field emission from conventional emitters will be outlined in this chapter. The equation relates the emitted current to the strength of the applied field, the work function φ and the Fermi energy μ. Existing measurements of field emission from carbon nanotube films fabricated by the surface decomposition of silicon carbide will be described and interpreted in terms of generalization of the Fowler-Nordheim theory to CNT emitters.

2.1 Fowler-Nordheim equation

Field emission, also known as Fowler-Nordheim tunneling, is the quantum mechanical process whereby electrons tunnel through a barrier in the presence of an electric field [8]. The efficiency of this emission process is much higher than all the other known emission processes such as thermionic emission [9].

In field emission, the strength of the applied electric field is usually on the order of 10^7 V/cm causing deformation of the image potential barrier so strongly that even electrons which are not excited can pass through it. An overview of the potential barrier narrowing phenomena due to applied voltage between the anode and the cathode is given in Fig. 7.

The image potential in Fig. 7 is a consequence of the electrostatic boundary conditions which require for an electron placed in front of a conducting surface to introduce a positive charge at the same distance behind the surface [8]. The three graphs, namely the image potential graph, the applied field and the resultant graph of the image class and the applied field has been plotted on different scale.

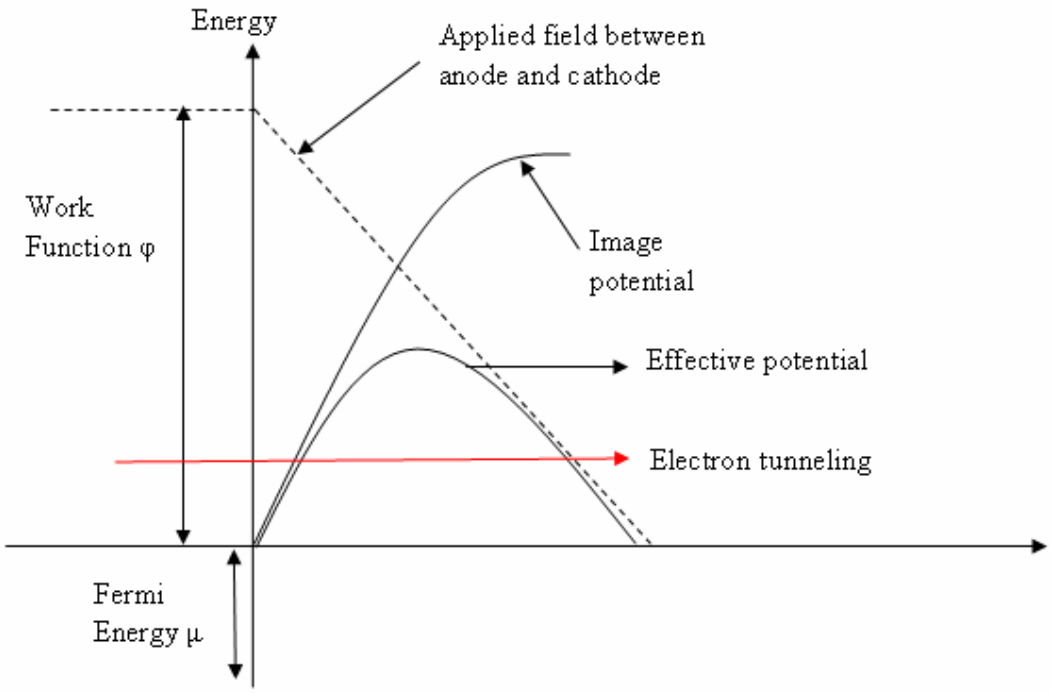

Fig. 7. Energy diagram for electrons at the metal surface in the presence of an applied field with image potential [8].

Let us consider an electron close to the Fermi energy μ. The work function φ of the metal corresponds to the energy difference between the Fermi energy μ and the field-free vacuum near the surface of the metal as shown in Fig. 8.

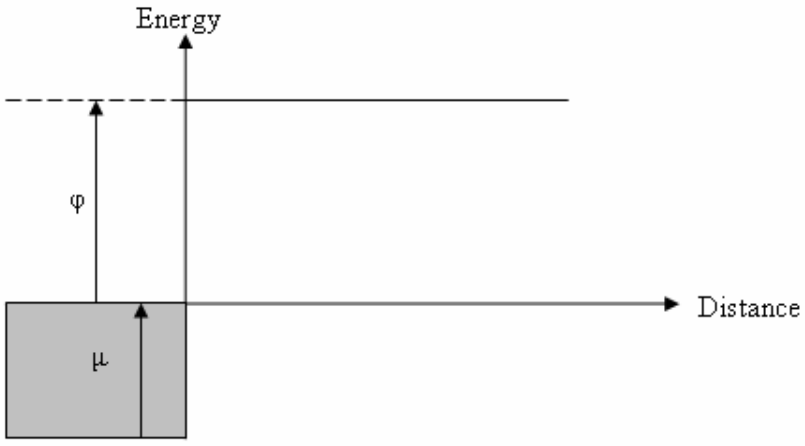

Fig. 8. Energy diagram for an electron in a metal with the Fermi energy μ and work function φ [8].

When an electric field $\mathbf{F}$ is applied to the metal surface, electrons of kinetic energy T_x along the emission direction come across a barrier of height $\varphi + \mu - T_x$ and the thickness of $(\varphi + \mu - T_x)/Fe$ [8]. Since tunneling is a quantum mechanical process, the Heisenberg uncertainty principle $\Delta X \Delta P \geq \hbar/2$ is used, where ΔX is the uncertainty in the position of the electron and ΔP is the uncertainty in the momentum of the electron. When an electron is close to the Fermi level, the kinetic energy that the electron needs to leave the metal is φ. Hence,

$$1/(2mv^2) = \varphi \text{ and } v = (2\varphi/m)^{1/2}, \tag{1}$$

and uncertainty in position is $\Delta X \approx \hbar/(2\Delta P) = \hbar/2(2m\varphi)^{1/2}$. The width of the barrier is given by $X = \varphi/Fe$. Since the barrier is very thin $\Delta X \approx X$ and $\varphi/(Fe) \approx \hbar/2(2m\varphi)^{1/2}$ or $2(2m)^{1/2}(\varphi)^{3/2}/Fe\hbar \approx 1$.

The transmission coefficient through a one-dimensional potential barrier by using Wentzel-Kramers-Brillouin (WKB) approximation is given by

$$D(E,V) = f(E,V)\exp[-2(2m/\hbar^2)^{1/2}\int_0^l (V-E)^{1/2}\, dx], \tag{2}$$

where $D(E,V)$ is the probability that the electron will tunnel through the barrier, V and E is the electron's potential and total energy, respectively and $f(E,V)$ is a constant.
The exponential part of $D(E,V)$ can be approximated by $[\psi(l)/\psi(0)]^2$, where $\psi(l)$ and $\psi(0)$ are the electron wavefunctions at $x = 0$ and $x = l$.
To prove this approximation, consider the following argument:
Over small distances where V can be considered as a constant, the electron wave function is given by $\psi(x) = \exp(ikx)$, where $k = P/\hbar = [2m(E - V)/\hbar^2]^{1/2}$. In the barrier region, $(E - V)$ is negative and hence $\psi = \exp[-(2m/\hbar^2)^{1/2}(V - E)^{1/2}x]$.

Therefore, $\psi(x + dx)/\psi(x) = \exp[-(2m/\hbar^2)^{1/2}(V - E)^{1/2}]\,dx$ and hence

$$\psi(l)/\psi(0) = \exp[-(2m/\hbar^2)^{1/2}\int_0^l (V-E)^{1/2}\, dx] \tag{3}$$

and

$$D(E,V) = f(E,V)\exp[-2(2m/\hbar^2)^{1/2}\int_0^l (V-E)^{1/2}\,dx]. \qquad (4)$$

The integral is equal to the area under the curve $(V-E)^{1/2}$ from x = 0 to x = l. This area can be approximated by a triangle with base $(\varphi + \mu - T_x)/Fe$ and height of $(\varphi + \mu - T_x)^{1/2}$. Hence, the area is given by $(\varphi + \mu - T_x)^{3/2}/(2Fe)$ and

$$D(E,V) = f(E,V)\exp[-(2m/\hbar^2)(\varphi+\mu-T_x)^{1/2}/Fe]. \qquad (5)$$

This equation is very similar to the following equation derived more rigorously by Fowler and Nordheim

$$D(E,V) = \left\{4[T_x(\varphi+\mu-T_x)]^{1/2}/(\varphi+\mu)\right\}\exp[-b(\varphi+\mu-T_x)/F],\ b = (32m/9\hbar^2e^2)^{1/2}\ . \qquad (6)$$

The most important quantity to be determined within this theory is the current density. It can be obtained by multiplying the transmission coefficient (Eq.(5)) by appropriate differential arrival rate and then integrating over the kinetic energy range $(0 \le T_x \le \mu)$[8].

At ordinary temperatures, emission comes mainly from the vicinity of the Fermi level, that is, $T_x \approx \mu$ and $\Delta = \mu - T_x$ is very small compared to φ. Hence, the term $[T_x(\varphi + \Delta)]^{1/2} \approx (\varphi\mu)^{1/2}$. The Fowler-Nordheim exponent can be expanded as follows

$$\begin{aligned}(b/F)(\varphi+\Delta)^{3/2} &= (b/F)\varphi^{3/2}(1+\Delta/\varphi)\\ &\cong (b/F)\varphi^{3/2} + (b/F)(3\varphi^{1/2}\Delta/2) \ \text{ as } \Delta/\varphi << 1.\end{aligned} \qquad (7)$$

Multiplying Eq.(5) by the differential arrival rate constant given by $4\pi me\Delta/\hbar^3$ and then integrating over $0 \le T_x \le \mu$ we obtain the current density

$$j = [16\pi me(\varphi\mu)^{1/2}/\hbar^3(\varphi+\mu)]\exp(-b\varphi^{3/2}/F)\int_0^\mu \exp[((3b\varphi^{1/2}\Delta)/2F)\Delta dT_x]. \qquad (8)$$

Since the region below T_x does not contribute to the field emission, the limit 0 in the integral can be replaced by $-\infty$. Upon integration, the Fowler-Nordheim equation is given by

$$j = 6.2\times10^{6}[(\varphi\,\mu)^{1/2}F^{2}/(\mu+\varphi)]\exp(-6.8\times10^{7}\,\varphi^{3/2}/F) \quad \text{A/cm}^2 \tag{9}$$

The current density of Eq.(9) is in A/cm^2 with energies in units of electron volts and F in volts per centimeter.

2.2 Field emission of carbon nanotubes

The main disadvantage of commonly used metal emitters is that their resistivity increases with the temperature. This causes heating during operation and eventually the emitter tip melts. The melting of the emitter tip changes its shape and alters the magnitude of the emitted current. The properties that make the CNT a better material for field emission are its nanosized diameter (nanosized radius of curvature) as well as its high mechanical strength, high thermal and electrical conductivity and good chemical and structural stability. Consequently, it can endure higher fields required for field emission. Field emission performances are also evaluated by comparing the current density, turn-on field and threshold field for the different types of emitters [10]. The turn-on field and threshold field are defined as the macroscopic fields needed to produce a current density of 10 $\mu A/cm^2$ and 10 mA/cm^2, respectively. Carbon nanotubes (single-walled, multi-walled, capped and uncapped) all have lower turn-on and threshold fields which allow larger field emission current densities in the range of 10^7-10^8 A/cm^2 in comparison to conventional field emitters.

The high electric field required for field emission is obtained close to surfaces of larger curvature such as a CNT sharp tip [11]. The electric field at the surface of a spherical tip of radius r is given by $F = V_0/r$ where V_0 is the applied potential. The electric field at a sharp conducting tip is $F = \beta V_0/r$, where β is the field enhancement factor, which depends on the geometry of the emitter. The small diameter r and elongated shape h of the carbon nanotube leads to a higher field enhancement factor

$$\beta = 1.2(2.15 + h/r)^{0.90}, \quad (10)$$

which quantifies the ability of CNT to amplify the electric field. The radius of the tip is larger for a capped (closed) CNT than uncapped ones which lead to a weaker electric field and lower emission current. It is in contrary to the case of an open (uncapped) CNT where the radius of the tip is small and the strength of the electric field is large, leading to the higher field emission current.

Besides the enhancement factor, the physical and chemical properties of the CNT themselves can also modify the field emission pattern. However, the influence of these properties is not clearly understood at the present time.

Fowler-Nordheim (Eq.(9)) shows that the emitted current depends on the local electric field F and the work function φ. Therefore, a variation in the shape or size of the emitter (field enhancement factor) and/or the chemical state of the surface has a strong impact on the emitted current [11,12]. As a result of that, the emitted current varies over several orders of magnitude for small variation in the radius of the carbon nanotube as shown in Fig. 9 [13].

Large variations in the field enhancement factor β are also observed in carbon nanotubes. The value of β was calculated for 40 individual nanotubes and the results were compared with the experimental data. Only 30% of the measurements were in agreement with the theoretical value (Fig. 10).

This shows that the emission process is highly sensitive to the exact structure of the tip as it approaches the nanoscale [13].

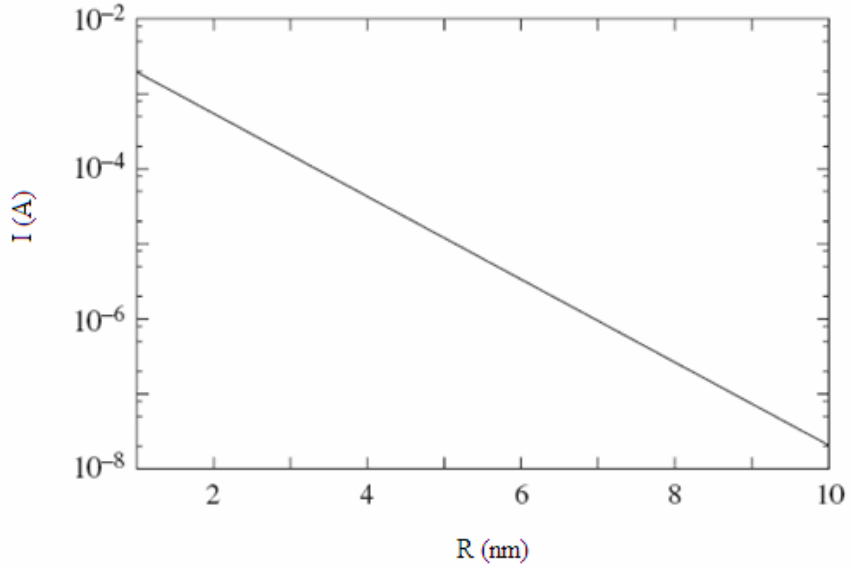

.

Fig. 9. Emitted current in a carbon nanotube with the Fowler-Nordheim theory as a function of radius with a work function of 5 eV, $\beta = 0.2$ and $V_0 = 300$ V [13].

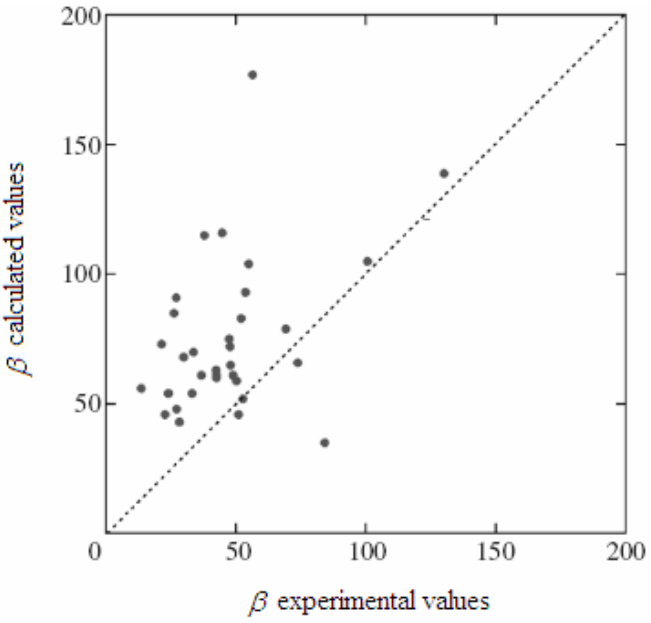

Fig. 10. Comparison between the field enhancement factor determined experimentally from Fowler-Nordheim plots and the theoretical field enhancement factor [13].

The main application of carbon field emitters is to manufacture field emission displays. Samsung demonstrated the first working carbon nanotube display prototype in 1999 by making a 30-inch screen [14]. Amaratunga reports that 38-inch color CNT cathode ray tube display consumes approximately 70 W, while a similar size plasma display consumes approximately 700 W, both for the same performance [15].

2.3 Field emission of carbon nanotubes grown by surface decomposition of SiC

Field emissions were done on CNT films formed by the surface decomposition method by Boeckl et al., [16] and Ito et al., [17] by measuring the turn-on voltage (electric field needed to produce a current of 10 $\mu A/cm^2$), threshold voltage (electric field needed to produce a current of 10 mA/cm^2) and the maximum current density.

Fowler-Nordheim plots were then drawn by Boeckl to find out whether the emitted current was the result of field emission. A Fowler-Nordheim plot is a graph of ln (I/V^2) versus (1/V). If a straight line graph is obtained, then it shows that the current is due to field emission. In some trials, the application of the electric field resulted in improved field emission in terms of a lower turn-on electric field and increased current density. However, on some of the trials, the field emission pattern deteriorated.

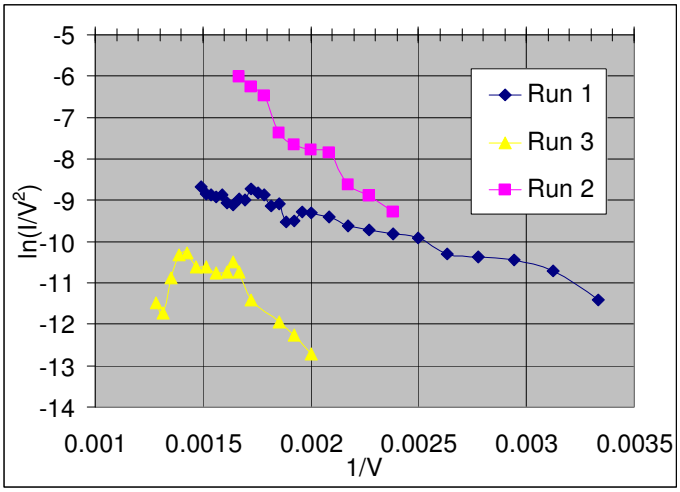

Fig. 11. Measured data plotted on a Fowler-Nordheim graph.

Run 1 performed by Boeckl et al., [16] showed a good field emission pattern with a low turn-on electric field of 54.8 μA/cm^2 at 3.0 V/μm and a maximum current density of 4.25 mA/cm^2 at 6.7 V/μm. However, run 2 and 3 indicated a deterioration of the field emission pattern. This could be explained by the presence of adsorbed impurities on the surface of the carbon nanotube film and these impurities causes a change in the work function of the CNT and hence explaining the instability in the field emission pattern. The presence of the adsorbed molecules was confirmed by X-ray photoelectron spectroscopy analysis. It shows the presence of graphitic carbon and a small amount of oxygen on the surface.

The carbon nanotube films were subjected to a post-growth treatment by Ito and collaborators [17]. The removal of the carbon nanotube caps were carried out in air at a temperature of 500-700^0 C. It was found that the removal of the carbon nanotube caps contributed to an increase in the total current. The turn-on voltage also decreased as shown in Fig. 12.

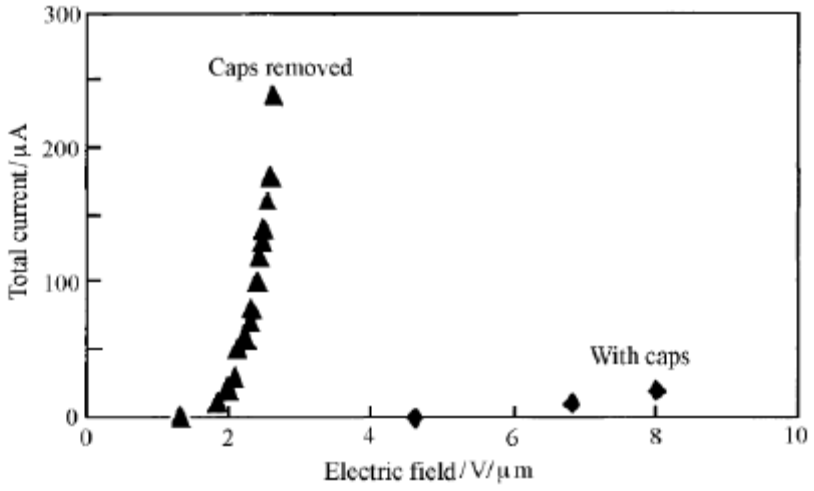

Fig. 12. Comparison of field emission characteristic of capped and uncapped carbon nanotubes grown by the surface decomposition of carbon nanotubes [17].

However, some papers have reported that open CNT have poor stability and emission pattern [18]. The poor stability is attributed to the presence of other species (such as oxygen molecules) that are attached to the free dangling bonds existing at the open end of the CNT. These molecules lead to the localization of the electron states and cause a deterioration of the field-emission pattern.

CHAPTER 3

EVANESCENT MICROWAVE MICROSCOPY

3.1 Introduction to evanescent microwave microscopy

There is an increasing demand to promote non-destructive and non-contact methods for determining the surface and subsurface properties of materials. Electromagnetic measurements are the foundation for emerging new technologies as well as improving the existing devices and processes. The electromagnetic properties of interest in characterizing materials are their local complex permittivity parameters, such as conductivity and dielectric constants.

A quantitative relationship between the real and imaginary part of local complex dielectric constant and frequency shift using the method of images is described in this chapter [19]. The extraction of quantitative data through evanescent microwave microscopy requires a detailed configuration of the field outside the probe-tip region. The solution to this field will relate the perturbed signal to the probe-tip-sample distance and the physical properties of the sample can then be determined.

In this experimental study, a near field microwave microscopy sensor was used to characterize the CNT samples through the frequency shift measurements of an evanescent microwave probe. The relative sensitivity of the microscope is in the range of 10^{-2} and the resolution is governed by the radius of the probe-tip [19]. The microwave probe consists of a tuned $\lambda/4$ coaxial transmission line with an end wall aperture as shown in Fig. 13. A TEM wave, created from a frequency generator moves along the coaxial probe and is totally internally reflected at the surface of the end wall aperture. The evanescent waves emanate off a sharpened tip extending concentrically through the aperture and interact with the sample. The coaxial microwave probe is coupled to the network analyzer through a tuning network and coupled to the sample as shown in Fig. 14.

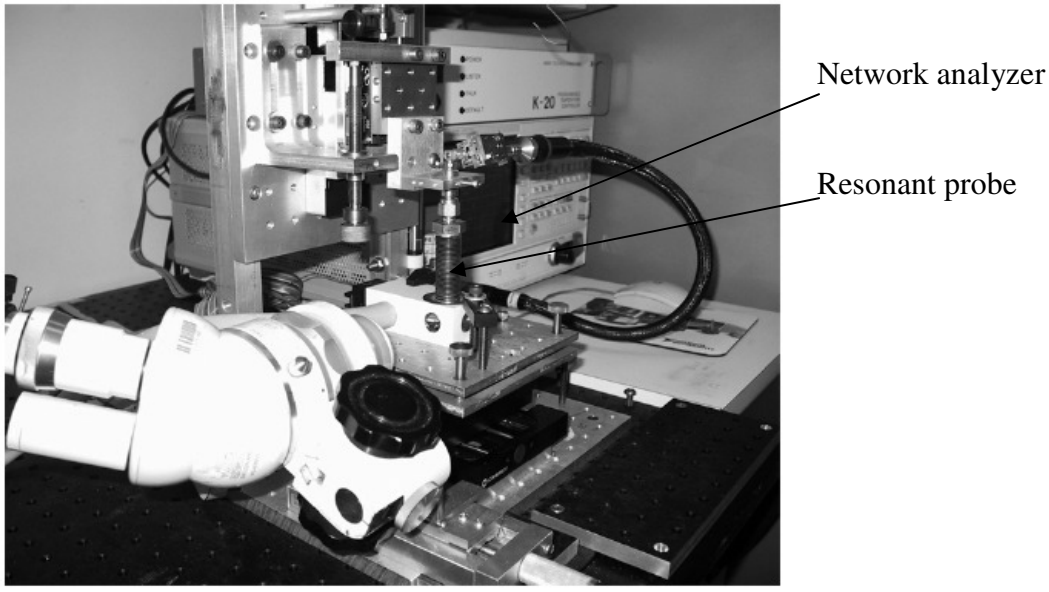

Fig. 13. Evanescent microwave microscopy system [19].

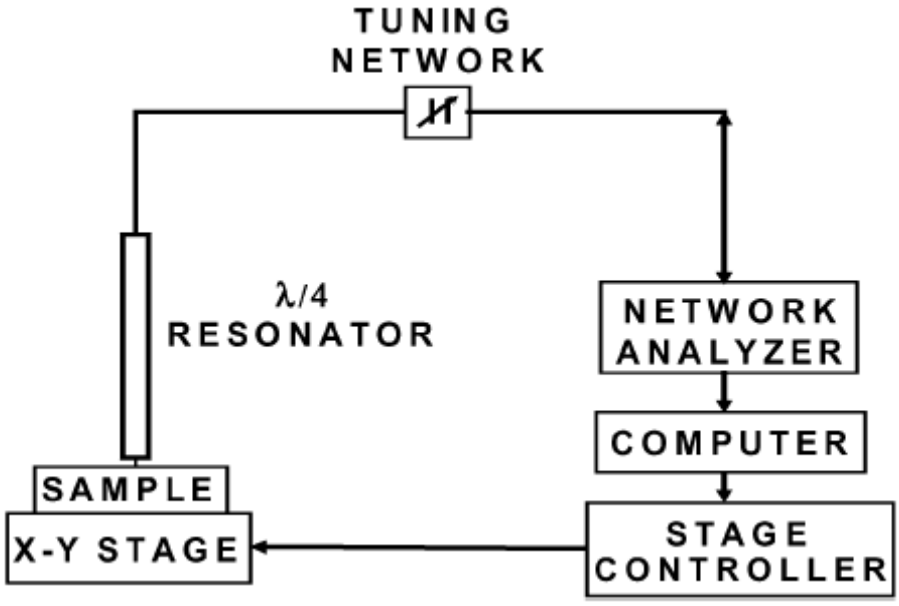

Fig. 14. Block diagram of the evanescent microwave microscopy system [19].

The probe can be operated in two different modes:

(1) It is capable of producing X-Y scans of the material properties if the air gap distance between tip and sample is held constant. The resonant frequency shift, Q-factor and the

reflection coefficient variations related to the physical properties of the sample surface can be mapped as the probe tip is scanned over some specific sample area [19]. The changes in the probe's resonant frequency, quality factor and reflection coefficient are tracked by a Hewlett-Packard 8722ES network analyzer (Fig. 14). The X-Y stage is driven by optical encoded, dc and linear actuators. The probe is frame mounted to a Z-axis linear actuator assembly and the height at which the probe is above the sample can be precisely set. The X-Y stage actuators, network analyzer, and the data acquisition and collection are computer controlled. The program that interfaces to the X-Y stage actuators, serial port communications, 8722ES GPIB interface, and the data acquisition is written in National Instruments Labview® software. The complete evanescent microwave scanning system is mounted on a vibration-dampening table.

(2) The system is also capable of determining local complex permittivity values for different materials by measuring the resonant frequency shift of the resonant coaxial probe as the tip approaches the sample surface. The resonant frequency data is produced by setting the reference resonant frequency at a distance above the sample surface and moving the probe tip in micrometer segments towards the sample to a distance of 1 μm from the surface. The resonant frequency reference of the probe is set at a fixed distance above the sample, which is approximately 15 μm. As the tip approaches the sample, it will interact with the evanescent wave. The resonant frequency shift data is best fit by a method of images model that produces the real and complex part of permittivity [19].

3.2 Description of theoretical model based on the method of images

In analyzing the electromagnetic properties of a material quantitatively, the probe-tip can be modeled as a conducting sphere with potential V_o placed above the sample causing a change in the field distribution when the tip is moved towards the sample. The method of images is applied to describe the redistribution of the electromagnetic field and it requires a series iteration of the two images as shown in Fig. 15 to preserve the boundary conditions.

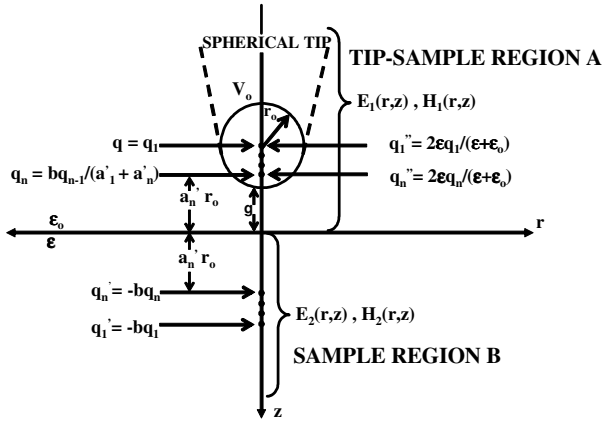

Fig. 15. Image charges (q, q', q") for spherical tip over sample [19].

For example, when we are dealing with a dielectric material, due to the location of the resonator tip close to the sample, the dielectric material will be polarized by the electric field. This interaction causes a redistribution of charge on the tip in order to maintain the equipotential surface of the sphere and leads to a shift in the frequency of the resonator [19].

In this model, the material perturbation theory for microwave resonators is applied, dealing only with the field distribution outside the tip. The derivation for the frequency shift for material perturbation [20] is given in the following section.

3.3 Derivation of frequency shift using material perturbation

Consider a resonator which has been perturbed by the presence of the sample in the vicinity of the resonator. Let $\mathbf{E}_0, \mathbf{H}_0$ be the fields of the original resonator and $\mathbf{E}, \mathbf{H}$ be the fields in the perturbed resonator. ω_0 and ω are the resonant frequencies in the unperturbed and perturbed resonator, respectively. Maxwell's equations can be written as

$$\nabla \times \mathbf{E}_0 = -i\omega_0 \mu \mathbf{H}_0, \tag{11}$$

$$\nabla \times \mathbf{H}_0 = i\omega_0 \mathbf{E}_0, \tag{12}$$
$$\nabla \times \mathbf{E} = -i\omega(\mu + \Delta\mu)\mathbf{H}, \tag{13}$$
$$\nabla \times \mathbf{H} = i\omega(\varepsilon + \Delta\varepsilon)\mathbf{E}. \tag{14}$$

Multiplying the complex conjugate of Eq.(11) by $\mathbf{H}$ and Eq.(14) by $\mathbf{E}_0^*$, we get

$$\mathbf{H}.\nabla \times \mathbf{E}_0^* = i\omega_0\mu\,\mathbf{H}.\mathbf{H}_0^*, \tag{15}$$
$$\mathbf{E}_0^*.\nabla \times \mathbf{H} = i\omega(\varepsilon + \Delta\varepsilon)\mathbf{E}_0^*.\mathbf{E}. \tag{16}$$

Subtracting these two equations and using the following vector identity,

$$\nabla.(\mathbf{A}\times\mathbf{B}) = \mathbf{B}.\nabla \times \mathbf{A} - \mathbf{A}.\nabla \times \mathbf{B}, \tag{17}$$

leads to the following equation

$$\nabla.(\mathbf{E}_0^*\times\mathbf{H}) = i\omega_0\mu\,\mathbf{H}.\mathbf{H}_0^* - i\omega(\varepsilon + \Delta\varepsilon)\mathbf{E}_0^*.\mathbf{E}. \tag{18}$$

Similarly, by multiplying the conjugate of Eq.(12) by $\mathbf{E}$ and Eq.(13) by $\mathbf{H}_0^*$ and using the vector identity in Eq.(17), we get the following equation,

$$\nabla.(\mathbf{E}\times\mathbf{H}_0^*) = -i\omega(\mu + \Delta\mu)\mathbf{H}_0^*.\mathbf{H} + i\omega_0\varepsilon\,\mathbf{E}_0^*.\mathbf{E}. \tag{19}$$

Addding Eq.(18) and Eq.(19) and integrating over volume V_0 and using the divergence theorem,

$$\int_{V_0} \nabla.(\mathbf{E}_0^*\times\mathbf{H} + \mathbf{E}\times\mathbf{H}_0^*)\,dV = \oint_{S_0} (\mathbf{E}_0^*\times\mathbf{H} + \mathbf{E}\times\mathbf{H}_0^*).d\mathbf{S} = 0$$
$$= i\int_{V_0} \{[\omega_0\varepsilon - \omega(\varepsilon + \Delta\varepsilon)]\mathbf{E}_0^*.\mathbf{E} + [\omega_0\mu - \omega(\mu + \Delta\mu)\mathbf{H}_0^*.\mathbf{H}\}dV, \tag{20}$$

where the surface integral is zero on S_o. This equation can be rewritten as

$$\frac{\Delta f}{f_0} = -\frac{\int_{V_0}[(\Delta\varepsilon)(\mathbf{E}.\mathbf{E}_0) + (\Delta\mu)(\mathbf{H}.\mathbf{H}_o)]dV}{\int_{V_0}\left(\varepsilon_0\mathbf{E}_0{}^2 + \mu_0\mathbf{H}_0{}^2\right)dV} = \frac{f - f_0}{f_0}, \tag{21}$$

V_0 is the volume of a region outside the resonator tip, f ($\omega = 2\pi f$) is the resonant frequency and f_0 ($\omega_0 = 2\pi f_0$) is the reference frequency.

From Fig. 15, the potential at any arbitrary points outside the sphere located at a distance **d** in cylindrical coordinates (r,θ,z) from the sphere centre will be used to solve for the unperturbed electric field. The distance d is given by $\mathbf{d} = r\hat{\mathbf{r}} + (z + r_0 + g)\hat{\mathbf{z}}$, with radius r_o of the spherical tip and g as the gap between the tip and surface of the sample.
The potential is given by

$$V(r,z) = \frac{q}{4\pi\varepsilon_0}\frac{1}{\left[r^2 + (z + a_1' r_0)^2\right]^{1/2}} \tag{22}$$

and the unperturbed field is given by the negative gradient of the potential V(r,z)

$$\mathbf{E}_0(r,z) = \frac{q}{4\pi\varepsilon_0}\frac{\left[r\hat{\mathbf{r}} + (z + a_1' r_0)\hat{\mathbf{z}}\right]}{\left[r^2 + (z + a_1' r_0)^2\right]^{3/2}} \ , \tag{23}$$

where $a_1' r_0 = r_0 + g$.

The potential V_o on the spherical tip is given by

$$V_0 = \frac{q}{4\pi\varepsilon_0 r_0} \ . \tag{24}$$

By using the method of images (Fig. 15), the perturbed electric field in the tip-sample region and the sample volume (where r_o is much smaller than the sample thickness) can be derived as [19]

$$\mathbf{E}_1(r,z) = \frac{q}{4\pi\varepsilon_0}\sum_{n=1}^{\infty} q_n \left\{ \frac{\left[r\hat{\mathbf{r}} + (z + a_n' r_0)\hat{\mathbf{z}}\right]}{\left[r^2 + (z + a_n' r_0)^2\right]^{3/2}} - b\frac{\left[r\hat{\mathbf{r}} + (z - a_n' r_0)\hat{\mathbf{z}}\right]}{\left[r^2 + (z - a_n' r_0)^2\right]^{3/2}} \right\} \ , \tag{25}$$

$$\mathbf{E}_2(r,z) = \frac{1}{2\pi(\varepsilon + \varepsilon_0)}\sum_{n=1}^{\infty} q_n \frac{\left[r\hat{\mathbf{r}} + (z + a_n' r_0)\hat{\mathbf{z}}\right]}{\left[r^2 + (z + a_n' r_0)^2\right]^{3/2}} \tag{26}$$

where

$$a_n' = a_1' - \frac{1}{a_1' + a_{n-1}'}, \quad q_n = t_n q, \tag{27}$$

$$t_n = \frac{b t_n}{a_1' + a_{n-1}'}, \qquad t_1 = 1, \tag{28}$$

$$b = \frac{\varepsilon - \varepsilon_0}{\varepsilon + \varepsilon_0}, \qquad \varepsilon = \varepsilon' + i\varepsilon'' \quad . \tag{29}$$

It is important to notice that for a tip placed in free space , $\varepsilon = \varepsilon_0$ at the location r = 0 and $z = -g - r_0$ and $\mathbf{E}_0 = \mathbf{E}_1 = \mathbf{E}_2$, thus confirming the asymptotic behavior in Eq.(23), Eq.(25) and Eq.(26). By integrating the unperturbed electric field in Eq.(23) and the perturbed electric fields in Eq.(25) and Eq.(26) over a region outside the spherical tip the frequency shift Eq.(21) becomes [19]

$$\left(\frac{\Delta f}{f_0}\right)_{total} = \left(\frac{\Delta f}{f_0}\right)_1 + \left(\frac{\Delta f}{f_0}\right)_2 = -A\sum_{n=1}^{\infty} t_n \left[1 - \frac{1}{2}(1-b)\frac{1}{a_1' + a_n'}\right] \tag{30}$$

where

$$\left(\frac{\Delta f}{f_0}\right)_1 = -A\sum_{n=1}^{\infty} t_n \left[1 - \frac{1}{2}(1+b)\frac{1}{a_1' + a_n'}\right] \quad \text{Reg. A}$$

$$\left(\frac{\Delta f}{f_0}\right)_2 = -A\sum_{n=1}^{\infty} t_n \left[\frac{b}{a_1' + a_n'}\right] \qquad \text{Reg. B}$$

$$\Delta\left(\frac{1}{Q}\right) = \frac{1}{Q} - \frac{1}{Q_0} = -(B + \tan\delta\, \frac{\Delta f}{f_0}) \tag{31}$$

Parameter A is a constant determined by the geometry of the tip-resonator assembly. Taking into account the real part of Eq.(30), we can fit this analytical expression, with our experimental data to find the real and imaginary parts of dielectric constant.

The model is utilized in the electromagnetic characterization of the CNT films to determine the real and imaginary component of the dielectric constant. The equations for

the change in the frequency and the Q-factor are derived, when the tip touches the sample.

CHAPTER 4

FABRICATION AND CHARACTERIZATION OF THE SAMPLES

4.1 Preparation of carbon nanotubes samples

A complete description of the preparation of the CNT samples, grown at Wright Patterson Air Force Base, will be given in this section. The information was obtained in a private conversation with Dr. J. Boeckl. It is very important to know the preparation conditions because physical properties of the samples can change depending on these conditions. Commercial grade 6H and 4H silicon carbide wafers, were mechanically polished and used to grow the carbon nanotubes films[21]. They were cleaned by a standard cleaning process developed by W. Kern while working for Radio Corporation of America and hence the name RCA cleaning treatment. The treatment consists of three major steps. First, the insoluble organic contaminants on the surface of the SiC wafer are removed by placing the wafer in a solution containing deionized water, hydrogen peroxide and ammonium hydroxide in a 5:1:1 ratio. The solution is prepared by heating the deionized water in a clean beaker up to 90^0 C, then adding the hydrogen peroxide and ammonium hydroxide. In the second step, the thin layer of silicon dioxide and contaminants from the first step have to be removed by using water and hydrogen fluoride solution. The solution consists of deionized water and hydrogen fluoride in a 50:1 ratio. In the last step, ionic and heavy metal contaminants have to be removed by using a solution containing water, hydrogen peroxide and hydrochloric acid in a 6:1:1 ratio. The sample is then placed in a graphite resistance furnace (Oxy-Gon Industries, Inc., Epsom, NH) at a temperature between 1400^0 C and 1700^0 C for 0.5-12 hours with a moderate vacuum pressure between 10^{-3} to 10^{-5} Torr [21] produced by a turbomolecular pump (Fig. 16). The samples that were prepared at 1700^0 C and under a pressure of 10^{-4} Torr are shown in Tab.III.

Tab.III. Samples fabricated by using the surface decomposition method.

Samples	Growth time (hrs.)	Quantity
C-face	1	3
Si-face	1	3
C-face	3	2
Si-face	3	4
C-face	6	3
Si-face	6	2

Fig. 16. A picture of the graphite resistance furnace used at Wright-Patterson Air Force Base to grow the carbon nanotubes.

The furnace is doubled-walled and electropolished to attain highest vacuum quality. Ports are incorporated in the heat chamber for a sight window, to insert thermocouples and for gas inflow. The temperature controller is programmable and the type of sensors used includes a thermocouple, an optical pyrometer and a transducer. The furnace is also equipped with a programmable logic controlled pumping system, which can operate in the range between 10^{-3} to 10^{-7} Torr.

A continuous film of vertically aligned carbon nanotube of thickness 250 nm was obtained for the carbon faced sample placed for 1 hour at 1700 ^{0}C. The CNT were both single and multi-walled. The diameter of the tube decreases with height and is wider at the interface between the SiC substrate and the CNT film. Graphitic carbon and a small amount of oxygen were also detected in the CNT films by X-ray photoelectron spectroscopy (XPS) [16]. The graphitic carbon is the residual carbon from the silicon carbide left on the surface of the carbon nanotubes after the preferential evaporation of silicon carbide. The silicon weight after decomposition was less than 1% of the film obtained. The CNT formed from the crystalline substrate were well-aligned and straight as shown in Fig. 17.

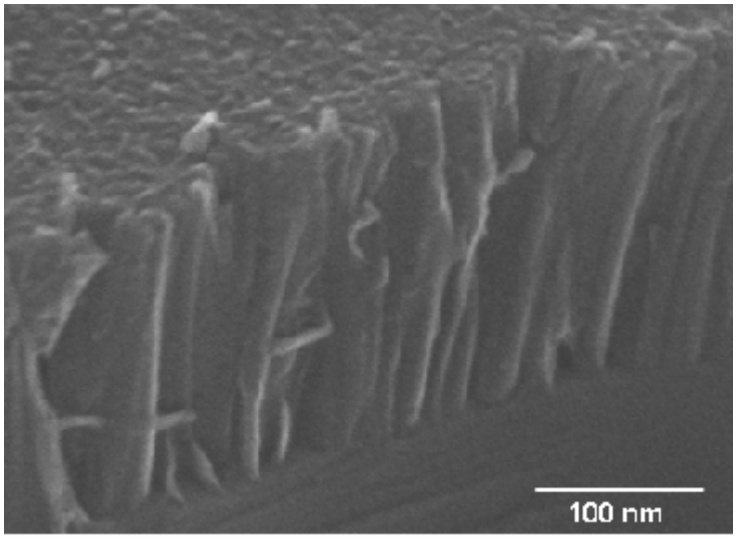

Fig. 17. A very dense film of aligned CNT, attached to the SiC substrate.

The height of the CNT is increasing almost linearly with growth time at 1700^{o} C and shown in Fig. 18 [21]. The length of the carbon nanotubes was approximately 300 nm on the silicon face and 500 nm on the carbon face respectively, for a 6 hour growth time. The rate of formation of CNT at the carbon face of the silicon carbide substrate is 1.5 times that on the silicon face. This difference in the formation rate of the CNT could be explained by the difference in the surface preparation and/or the presence of a thin oxide layer on the silicon terminated face.

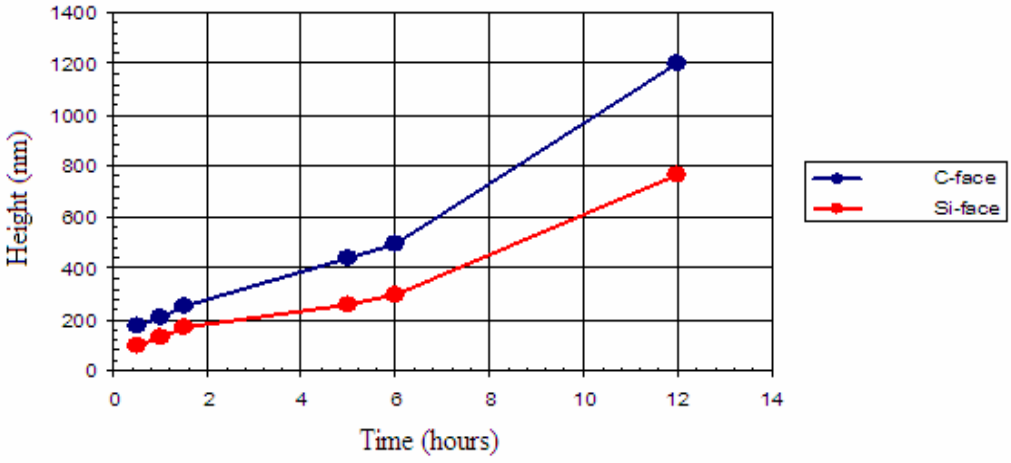

Fig. 18. Variation in height of the CNT with increasing growth time.

4.2 Post-growth treatment to uncap CNT

The post-growth treatment to uncap the CNT films was carried out in the Lab at Wright State University. The removal of the CNT caps was carried out by placing the sample in a box furnace at 400^0 C under oxygen or carbon dioxide flow at a pressure of 2 psi (Fig.20(a)). We also verified that a higher temperature can be used for this process but the dwelling time is shorter to obtain the same results. A type 30400 box furnace with a programmable Thermolyne temperature controller with four electric resistive heaters embedded in ceramic fiber refractory insulation is used for the post-growth treatment. When the furnace was switched on, the gas flow was adjusted to 2 psi. The setpoint on the temperature controller was 400^0 C and as a result of that the temperature was ramped automatically to 400^0 C within 1 hour in initial pre-heating stage of our experiment. The temperature in the box furnace was measured using a K-type thermocouple which has a temperature range from -200^0 C to 1200^0 C. A thermocouple wire connected to a separate thermocouple meter was placed next to the sample holder to monitor the temperature in the sample vicinity. The temperatures displayed on the programmable temperature controller and the thermocouple meter were in good agreement with one another (within $\pm 5^0$ C). A gas deflector was also placed to ensure

that the gas will be directed towards the sample. The sample was inserted into the furnace when the temperature on both the thermocouple and the controller was 400^0 C ± 5^0 C (Fig.20(b)). The temperature usually decreased to 380^0 C when the door of the furnace was opened and as soon as the door was closed, the temperature reached 400^0 C within 3 minutes. The samples were dwelled in the furnace for 25, 40 or 60 minutes under oxygen or carbon dioxide flow at this temperature. The door of the furnace was opened and the CNT were allowed to cool slowly under oxygen or carbon dioxide flow after the annealing process was completed. The samples were removed after 1 hour from the furnace when the temperature on both meters were 100^0 C and Tab. IV shows the list of the samples which we were chosen for the demonstration of the uncapping procedure.

Tab. IV. The post-growth treatment used for the several CNT samples.

<table>
<tr><th>Sample</th><th>Dwelling time (min.) at 400^0 C</th><th>Cooling conditions</th></tr>
<tr><td>C-face (3 hrs.)</td><td>25</td><td>Sample removed immediately.</td></tr>
<tr><td>C-face (3 hrs.)</td><td>25</td><td>Oxygen gas flow for 1 hour.</td></tr>
<tr><td>Si-face (3 hrs.)</td><td>25</td><td>Oxygen gas flow turned off.</td></tr>
<tr><td rowspan="3">Si-face (3 hrs.)</td><td>25</td><td rowspan="3">Oxygen gas flow for 1 hour.</td></tr>
<tr><td>40</td></tr>
<tr><td>60</td></tr>
<tr><td rowspan="3">Si-face (6 hrs.)</td><td>25</td><td rowspan="3">Carbon dioxide gas flow for 1 hour.</td></tr>
<tr><td>40</td></tr>
<tr><td>60</td></tr>
</table>

Fig. 19(a). Thermolyne furnace.

Fig. 20(b). Sample holder and gas deflector inside furnace.

After each step of the uncapping procedure and before and after annealing process, our samples were subjected to structural, chemical and physical analyses. SEM, TEM, AFM, XRD, EDS and evanescent microwave measurements were carried out for the samples listed in Tab. IV.

Samples with a growth time of 1 hour were not subjected to the post-growth treatment because of the short length of the CNT and short annealing time to remove them from the silicon carbide substrate. The contribution of the silicon carbide substrate will be more pronounced for this case and is not the objective of this study.

4.3 Structural and chemical characterization

The structural characterization of the CNT grown by surface decomposition was performed by collaborators at Wright Patterson Air Force Base to know the size distribution, alignment, periodicity and density of the CNT. This has been achieved by performing scanning electron microscope (SEM), transmission electron microscope (TEM) and atomic force microscope (AFM) analyses. Energy-dispersive X-ray spectroscopy (EDS) was performed to determine the chemical composition of the

samples and X-ray diffraction (XRD) patterns were used to determine the structure and the crystallinity of the sample.

4.3.1 Scanning Electron Microscope Analysis

The scanning electron microscope provides greater spatial resolution and depth of focus than optical microscope. The SEM can provide nanometer-level resolution up to 1,000,000 times in magnification. This is a non-destructive technique where primary electron beam is scanned over the surface of the samples. Different phenomena such as generation of secondary electrons (SE), backscattering of the secondary electrons (BSE) and emission of X-ray take place in the sample [22]. The signals generated by these processes are used by the corresponding detectors for image formation. SE are emitted from the uppermost surface of the sample. The emission intensity depends on the topography and the composition of the sample surface. Secondary electrons (BSE) are emitted from the sample due to elastic collision with the primary electrons. The intensity of the image depends on the average atomic number on the area. Inelastic scattering of the incident electrons produce the emission of X-ray with energies characteristic of the atoms in the specimen. A FEI Sirion Field-Emission system (Fig. 20) equipped with SE, BSE and X-ray detectors was used to analyze CNT samples. It has a spatial resolution of 5 nm along the X and Y direction.

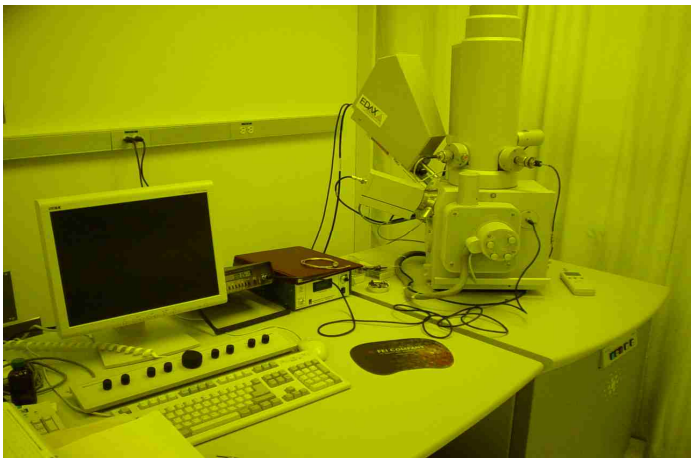

Fig. 20. FEI Sirion system used to obtain SEM images.

SEM analysis was carried out on our samples listed in Tab.III.

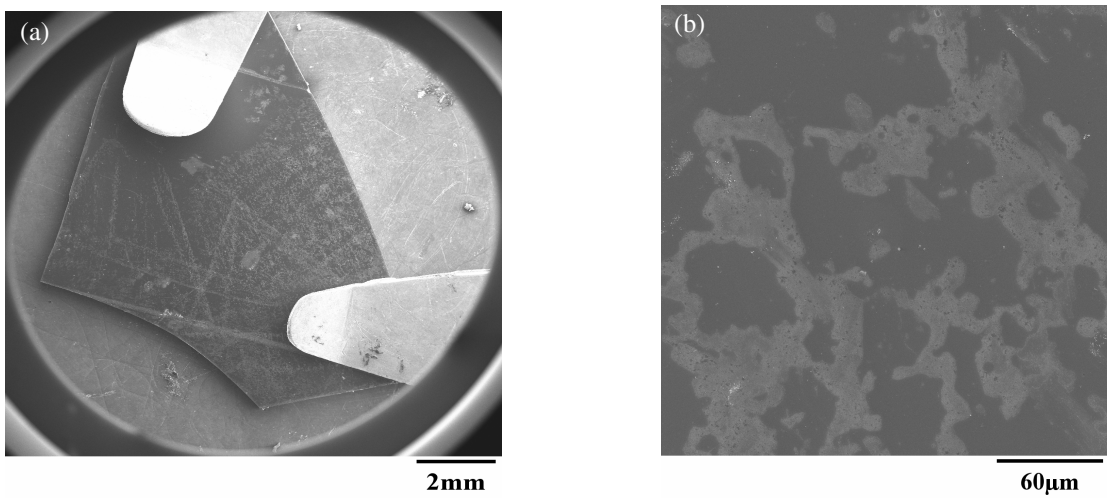

.

Fig. 21(a),(b). SEM images of the untreated C-face (3 hrs.) sample.

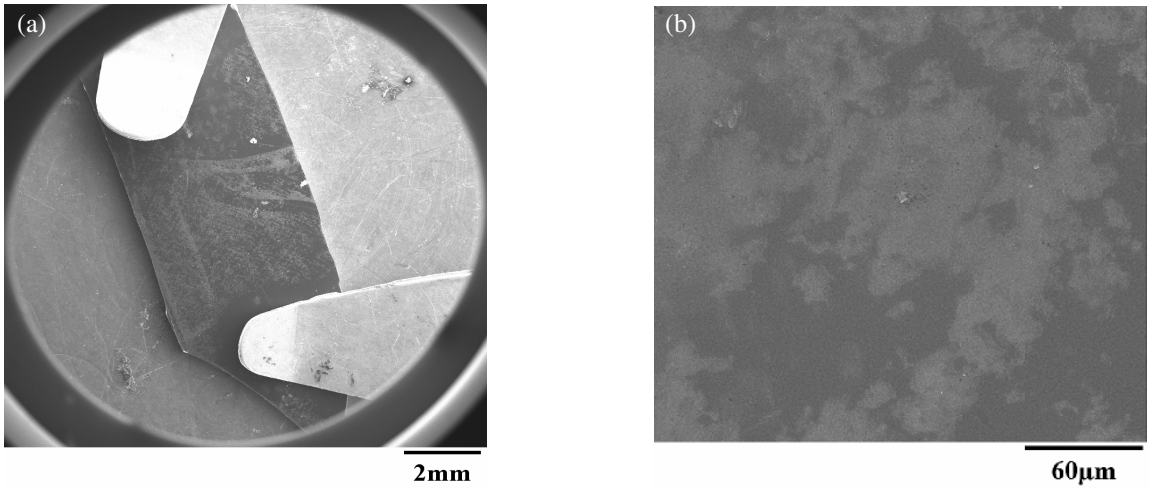

Fig. 22 (a),(b). SEM images of the untreated Si-face (6 hrs.) sample.

The SEM pictures (Fig. 21 and Fig. 22) show the presence of whitish patches on the surface. The presence of these white patches is due to the formation of amorphous carbon on the surface of the sample formed during the ramping up of the temperature to 1700^0 C and/or the presence of adsorbents such as oxygen that have adhered on the surface following the samples removal from the furnace. SEM analysis was performed also after the annealing process.

As an example, a SEM image of the cross-section of the CNT film formed after 30 min. annealing of silicon carbide substrate is shown in Fig. 23. A very dense film of both single-walled and multi-walled CNT that are well-attached to the substrate is shown. The CNT films are vertically aligned. In this particular picture, the top surface of the sample shows the coalescence of the carbon nanotubes due to accumulation of amorphous carbon leading to a continuous local surface. The CNT are roughly 250 nm high.

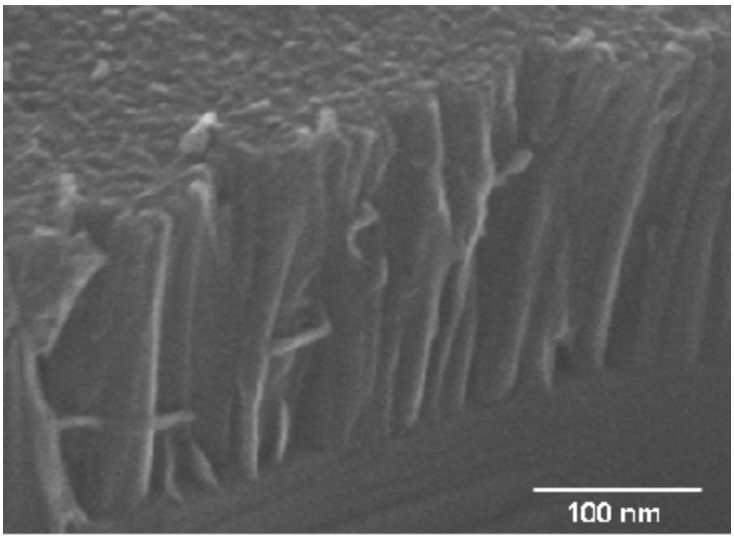

Fig. 23. Cross-sectional SEM image of the CNT grown at 1700^0 C for 30 min.

4.3.2 Transmission Electron Microcopy

Transmission electron microscope (TEM) is used to analyze the atomic structure and microstructure of solid materials by the diffraction of highly focused, non-energetic electrons that bombard a thin specimen of material. A TEM system is capable of imaging a thin-film sample and it shows the variation in mass, non-uniformity in sample thickness and structural defects in crystalline materials. The typical resolution is less than 0.2 nm. TEM analysis requires a sample which is usually less than 200 μm thick and is destructive due to sample preparation. Specimens for cross-sectional TEM studies were

prepared from representative samples using a focused Ga^+ ion beam (FIB) to cut thin foils perpendicular to the (0001) substrate orientation. These cross-section slices were thinned further by focused ion beam polishing followed by Ar-ion milling to electron transparency. Electron diffraction patterns and bright field images were then obtained from these thinned foils using a Philips CM-200 field emission gun (FEG) TEM operated at 200 kV (Fig. 24). Fig. 25 and Fig. 26 show a cross-sectional view and top view of the CNT images obtained by TEM.

Fig. 24. Philips CM-200 field emission gun (FEG) TEM operated at 200 kV.

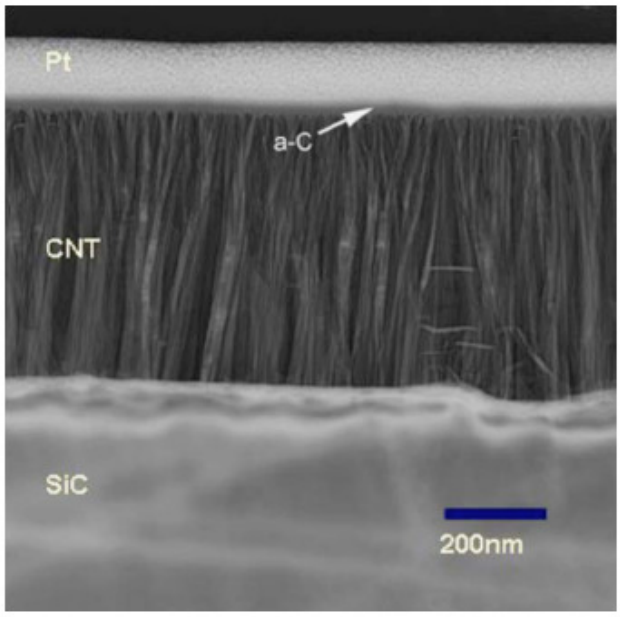

Fig. 25. Cross-sectional view of the TEM image of the CNT.

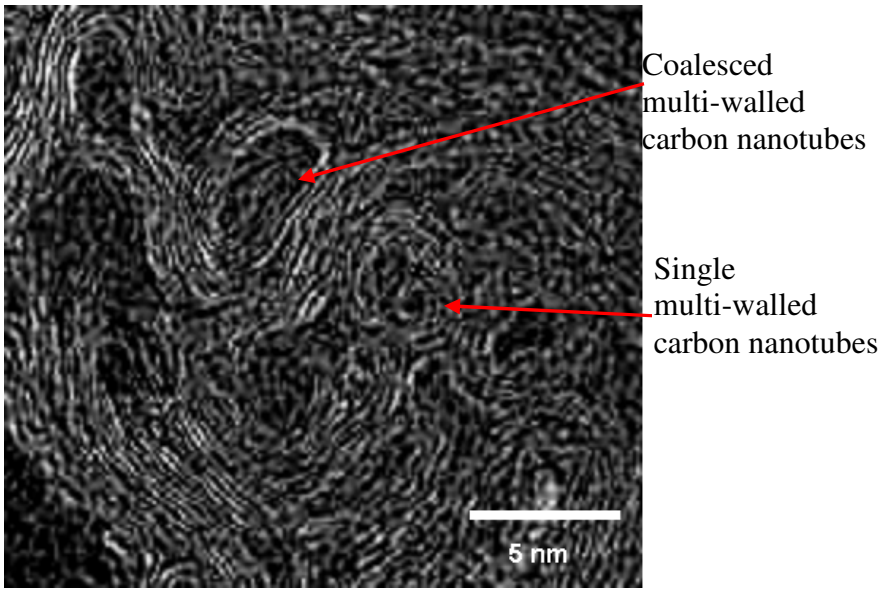

Fig. 26. Top-view of the TEM image of the CNT.

4.3.3 Atomic Force Microscopy

The atomic force microscope (AFM) is a high-resolution scanning probe microscope, which can resolve features down to fractions of a nanometer (Fig. 27).

Fig. 27. Veeco multimode V AFM/SPM

The operation of the AFM is based on the measurement of the forces between the sharp tip of the probe which is attached to a cantilever spring and the sample surface. The AFM can be operated in three different modes, namely, the contact mode, non-contact mode and the tapping mode. Fig. 28 shows an AFM image of the CNT film obtained by the tapping mode.

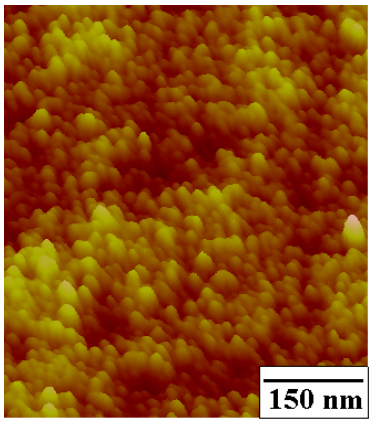

Fig. 28. AFM image of the CNT film.

4.3.4 X-Ray Diffraction

X-ray diffraction can be used to identify the crystalline phase, orientation and size of films. XRD systems radiate the specimen with a collimated beam of X-rays. Crystalline materials will diffract X-ray radiation according to Bragg's law, $\lambda = 2d \sin \theta$ where d is the distance between crystal planes, λ is the wavelength of the X-ray radiation and θ is the diffraction angle.

XRD systems measure the intensity of the diffracted X-ray radiation as a function of twice the off normal incidence diffraction angle θ. The penetration depth of the X-ray radiation is material and X-ray radiation source dependent. However, the penetration depth is typically limited to a few micrometers and is usually non-destructive. A Rigaku single crystal X-ray diffractometer (Fig. 29), which has a rotating anode X-ray source and an image plate detector system, was used to collect the X-ray of the CNT films.

Fig. 29. Rigaku X-ray diffractometer.

As an example, X-ray measurements were made for the untreated C-face (1 hr.) and the untreated C-face (6 hrs.) samples. An XRD pattern was produced with two significant peaks of intensity close to 120,000 counts and was identified as silicon carbide peaks for the untreated C-face (1 hr.) film (Fig. 30). After magnification adjustments (Fig. 31), there are also several peaks with a maximum intensity about 800 counts which have been identified as crystalline pure carbon (CNT). It confirms that for the 1 hr. growth time, only a small fraction of the silicon carbide substrate was converted into

CNT. As the growth time increases, the carbon peak intensities increase to the extent that the SiC peaks are no longer present in XRD pattern (Fig. 32).

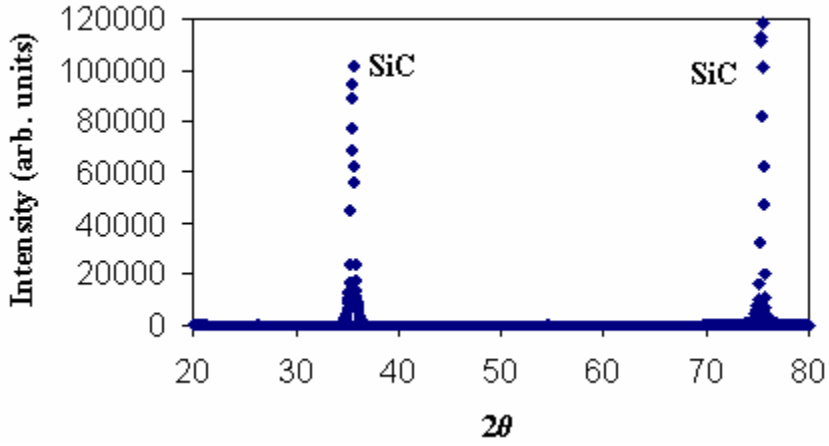

Fig. 30. X-ray pattern for the C-face (1hr.) sample.

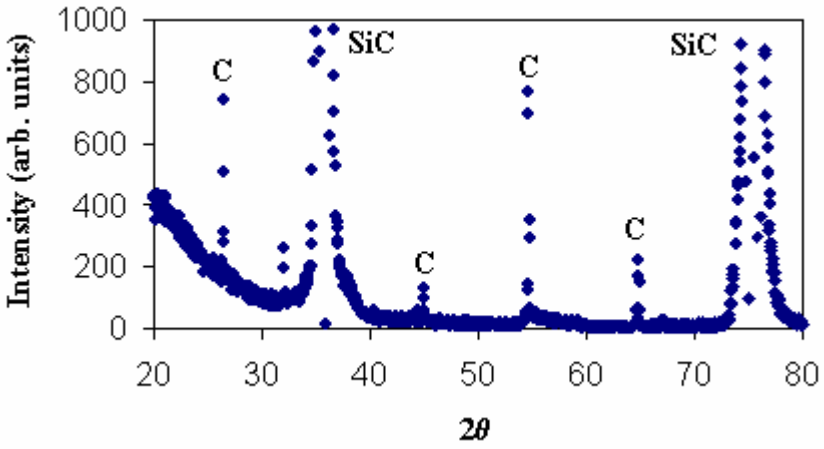

Fig. 31. X-ray pattern for the C-face (1 hr.) sample.

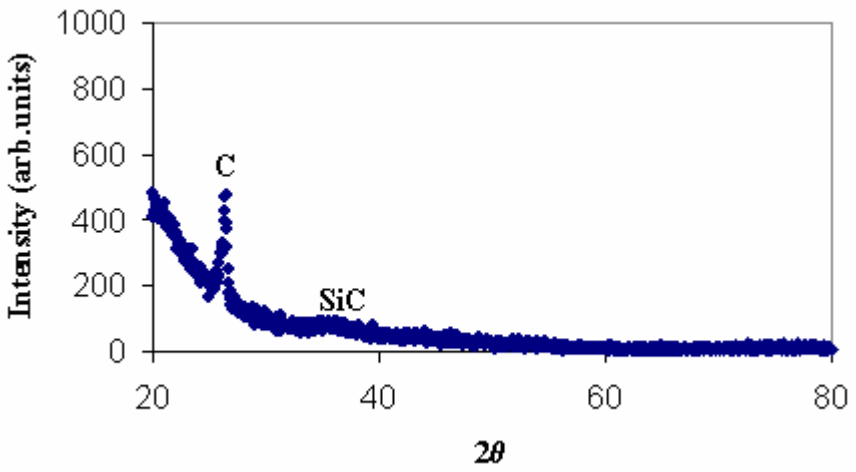

Fig. 32. X-ray pattern for the C-face (6 hr.) sample.

4.3.5 Energy-Dispersive X-Ray Spectroscopy

The collection and energy detection of X-ray spectra from a sample is defined as energy-dispersive X-ray spectroscopy. Atoms emit characteristic X-rays when ionized with high radiation energy. EDS analysis of the collected X-ray spectra is used to determine elemental composition of the sample.

A TEM/EDS system was used to determine the percentage composition of the SiC substrate before and after the growth of the CNT to compare the change in the composition of the sample. Fig. 33 shows the elemental analysis for CNT grown for 30 min. on a SiC substrate at 1700^0 C and for SiC prior to growth of CNT.

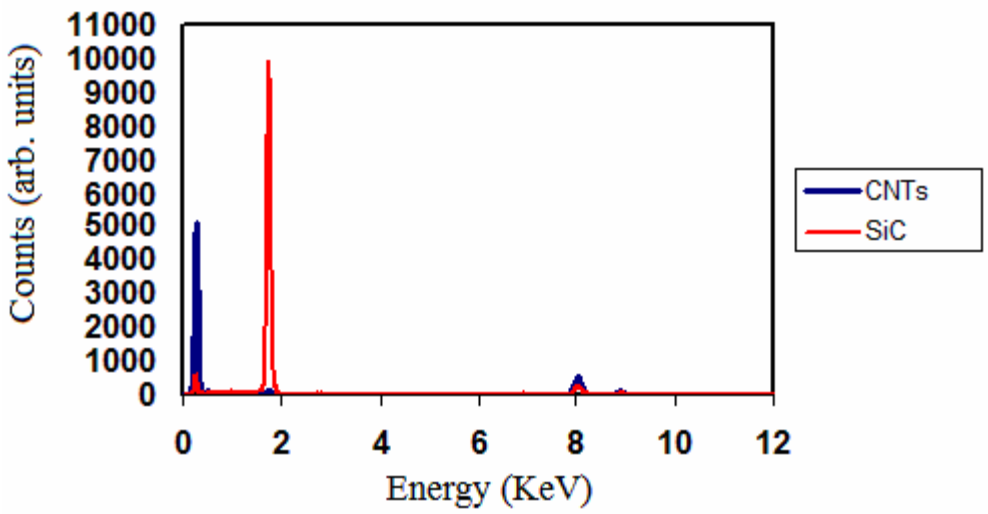

Fig. 33. EDS spectrum of the SiC before and after the growth of the CNT.

The quantitative percentage composition of the wafer before and after the growth of the CNT is shown in Tab.V.

Quantitative for SiC bulk		
Element	Wt %	Atom %
Si-K	63.08	42.21
C-K	36.92	57.79

(a)

Quantitative for CNT layer		
Element	Wt %	Atom %
Si-K	0.17	0.07
C-K	99.83	99.93

(b)

Tab.V. Elemental chemical analysis of SiC without (a) and with (b) CNT layer.

The data shows that silicon carbide has 63.08 % of silicon and 36.92 % of carbon by weight. After the growth of the CNT, the silicon percentage decreases drastically to 0.17 % by weight and the carbon weight increases to 99.83 %. This shows that most of the SiC decomposes to form CNT.

Also Leica 430i equipped with X-ray detector (Fig. 34) was used to obtain the elemental analysis of several untreated CNT films shown in Fig. 35 , Fig. 36 and Fig. 37. The typical lateral resolution of the system is 0.5 μm to 1 μm. The depth penetration is

dependent upon the density of the sample and the intensity of the radiation source. EDS can detect a range of elements from boron to uranium.

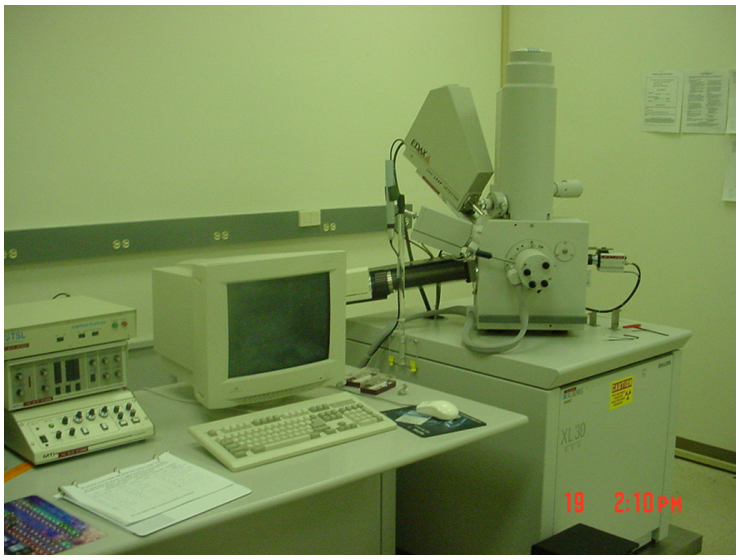

Fig. 34. Leica system used to obtain the EDS spectra.

Measurements were made on the C-face (1 hr.), C-face (3 hrs.), C-face (6 hrs.), Si-face (1 hr.), Si-face (3 hrs.) and Si-face (6 hrs.). The selective experimental results for the C-face (1 hr.), C-face (3 hrs.) and C-face (6 hrs.) are shown in Fig. 35, Fig. 36 and Fig. 37, respectively.

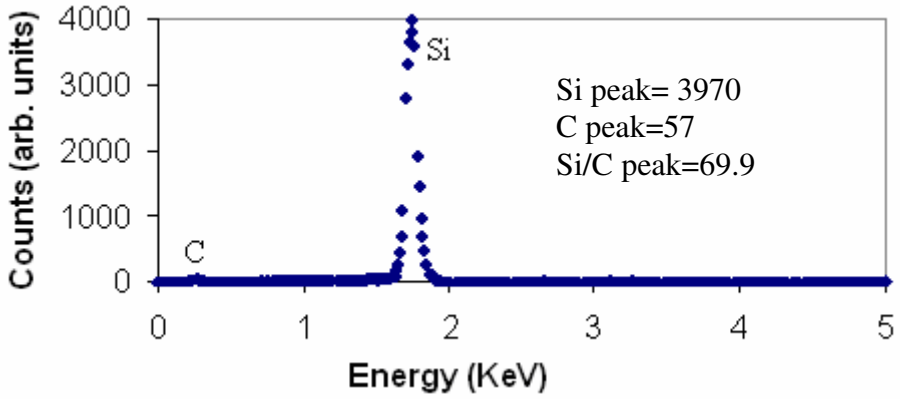

Fig. 35. EDS spectrum for C-face (1 hr.).

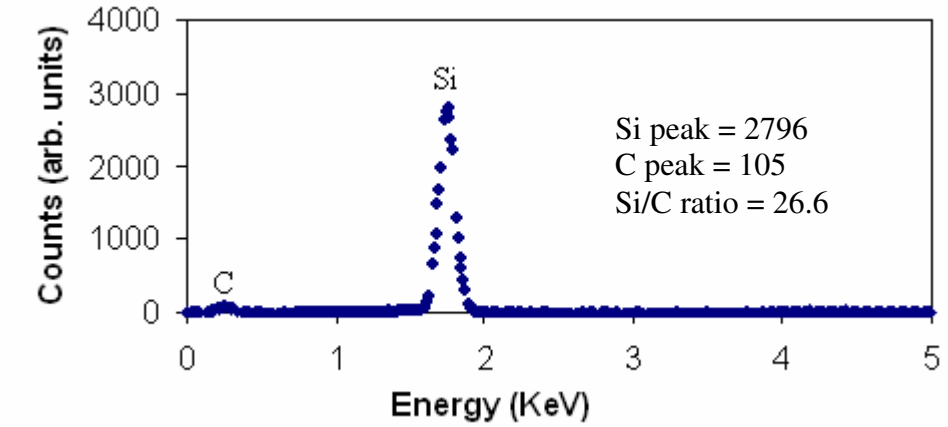

Fig. 36. EDS spectrum for C-face (3 hrs.).

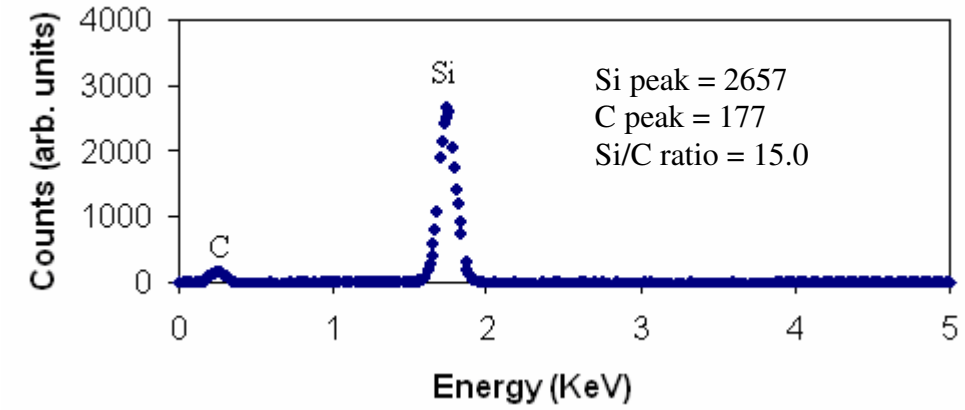

Fig. 37. EDS spectrum for C-face (6 hrs.).

The variation of the carbon peak intensity with growth time is summarized in Fig. 38 for the CNT grown on the C-face and Si-face of silicon carbide substrates.

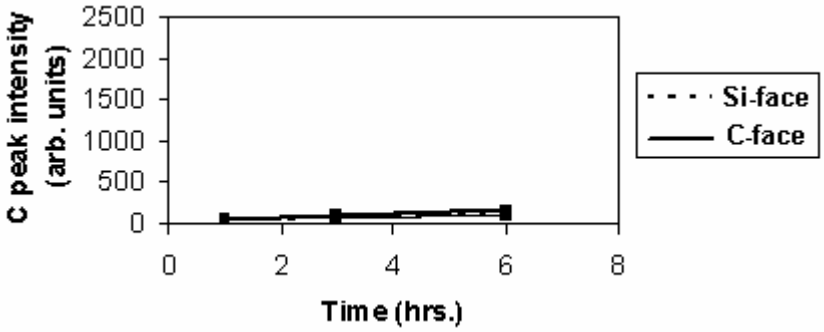

Fig. 38. Variation of C-peak intensity with growth time on the SiC substrate.

The variation of the silicon peak intensity with growth time is summarized in Fig. 39 for the CNT grown on the C-face and Si-face of silicon carbide substrates.

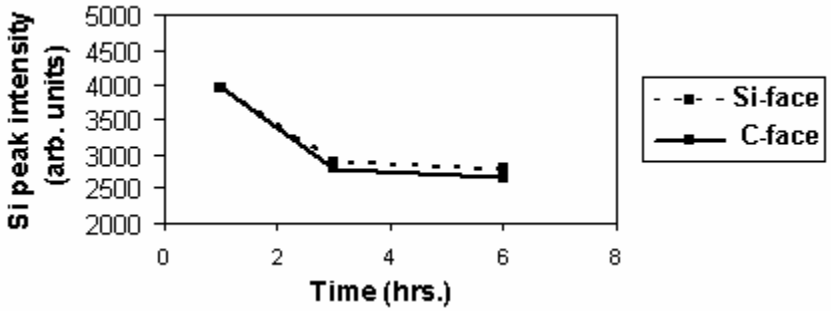

Fig. 39. Variation of the Si-peak intensity with growth time of the SiC substrate.

The ratio of the Si/C peak intensity was plotted against growth time. The graph of Fig. 40 shows that the rate of decomposition on the C-face is faster than that on the Si-face. This is due to the presence of the thin oxide layer on the surface of the Si-face of the substrate. The oxide layer hinders the quick decomposition of the silicon carbide on the Si-face.

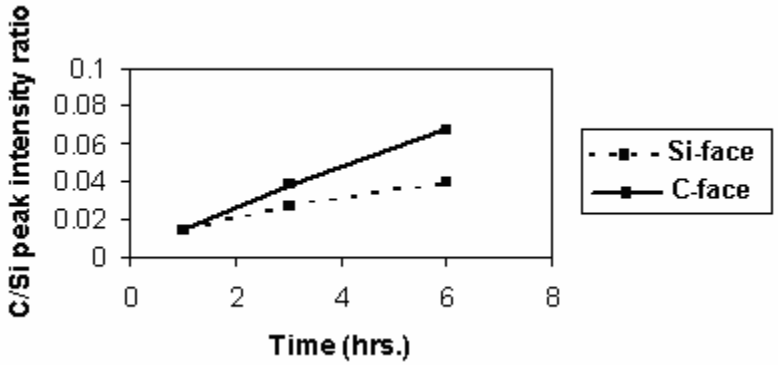

Fig. 40. Variation of the Si/C peak with growth time of the SiC substrate.

CHAPTER 5

FORMATION MECHANISM OF CARBON NANOTUBES GROWN BY SURFACE DECOMPOSITION OF SILICON CARBIDE

5.1 Introduction

The formation mechanism of carbon nanotubes fabricated by the surface decomposition of silicon carbide crystal on the silicon and carbon terminated face will be described in this chapter.

The carbon nanotubes can be grown by arc-discharge, laser ablation and chemical vapor deposition. Kusunoki et al., [23] found a new synthesis to grow CNT called surface decomposition of silicon carbide. The CNT grow in a vertical direction, eroding the SiC crystal during continuous oxidation. This new technique has one major advantage over traditional techniques mainly the latter one does not require nucleation sites. In arc-discharge, chemical vapor deposition or laser ablation, magnetic nanoparticles are used as catalysts and have to be removed at the end of the synthesis process. The purification techniques, involved in the removal of the catalyst impurities are usually tedious, expensive and cause degradation of the CNT. In surface decomposition, the CNT are grown without catalytic help. Kusunoki et al.,[24] reported the growth of CNT on the C-face (0001) of the silicon carbide only whereas thin graphite sheets were formed on the Si-face (0001). However, Boeckl et al., [21] and Nagano et al., [25] observed CNT growth on both the Si-face (0001) and the C-face (0001). The presence of the oxide layer on the Si-face delays the CNT formation.

5.2 Surface decomposition of silicon carbide

Surface decomposition is a simple technique that can be used to produce high purity and uniform CNT. The SiC has a hexagonal lattice with alternating hexagonal planes of silicon and carbon atoms. Each silicon atom bonds to four nearest neighbor carbon atoms and each carbon atom bonds to four nearest neighbor silicon atom as shown in Fig. 41.

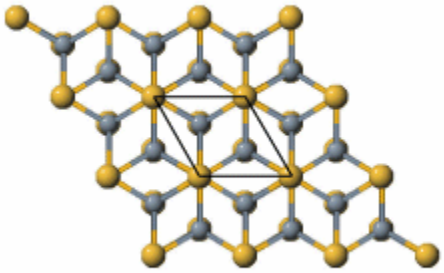

Fig. 41. Hexagonal structure of silicon carbide.

The SiC substrate is placed in a vacuum electric furnace at high temperature, usually in the range of 1300^0 C to 1700^0 C and at a pressure of 10^{-4} Torr. In order to understand the reaction mechanism, the substrates were heated at 1300^0 C and 1500^0 C for 0.5 hours at a pressure of 10^{-4} Torr. At 1300^0 C, the presence of small caps on the order 2-5 nm in diameter were observed along with graphite sheets parallel to the surface of the substrate. This is the initial stage of organization of the CNT film and experiments show that the size of the caps generated at this stage determines the diameter of the CNT. The 50 nm long CNT were observed at a temperature of 1500^0 C. If the pressure is decreased to 10^{-6} Torr, the lengths of the CNT were reduced to 25 nm. These results give a clear indication that the length of the CNT can be adjusted by varying the temperature, time of growth and pressure.

The proposed reaction mechanism is as follows

$$SiC_{(s)} + \frac{1}{2}O_{2(g)} \rightarrow SiO_{(g)} + C_{(s)} \tag{32}$$

or /and

$$SiC \rightarrow Si_{(g)} + C_{(g)} \tag{33}$$

In reaction (32), the oxygen present in the chamber oxidizes the silicon carbide to produce silicon oxide gas, leaving behind solid carbon, which forms the CNT [23].

The growth mechanism of the carbon nanotube films on SiC (0001) was studied using cross-sectional high resolution electron microscopy (HREM) [23]. Commercial SiC substrate with a polished Si (0001) and C (0001) face was placed in a furnace at a temperature of 1250^{o} C for 0.5 hrs. Four layers of slightly arched graphite sheets having an outer diameter of 5 nm and a height of 1-2 nm were found on the surface of the substrate. This is the initial stage of decomposition on the C-face which can be explained chemically as follows:

The carbon atoms in the first layer become free and do not retain any bonding with the surface (Fig. 42) as the silicon atoms evaporate when the substrate is heated above 1000^{o} C. The free carbon atoms agglomerate easily to form graphite sheets parallel to the top surface of the substrate [26].

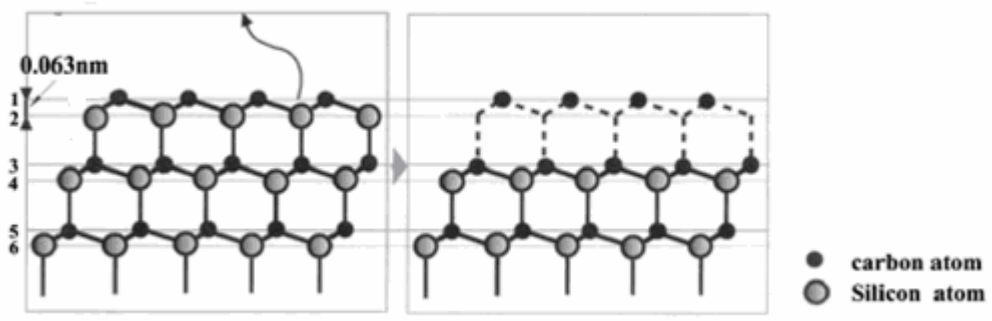

Fig. 42. The decomposition process on the C-face with the evaporation of the silicon atom [26].

At the higher temperature, the carbon-carbon (C-C) bonds in the graphite sheets undergo partial oxidation and begin to weaken, allowing the oxygen molecules to penetrate the surface of the silicon carbide. Silicon atoms, more reactive than carbon atoms, oxidize preferentially to form SiO gas as shown in Eq.(28). This causes the gap at the SiC/graphite interface to increase and the graphite sheets become arched. As the temperature of the sample is raised to 1300^{o} C, two to three layered carbon nanocaps, having a diameter of 3-5 nm and a height of 3-5 nm were formed at several places on the surface of the substrate as shown in Fig. 43(b). The SiO gas pressure caused the deformation of the graphite sheets leading to the formation of the nanocaps as shown in Fig. 43.

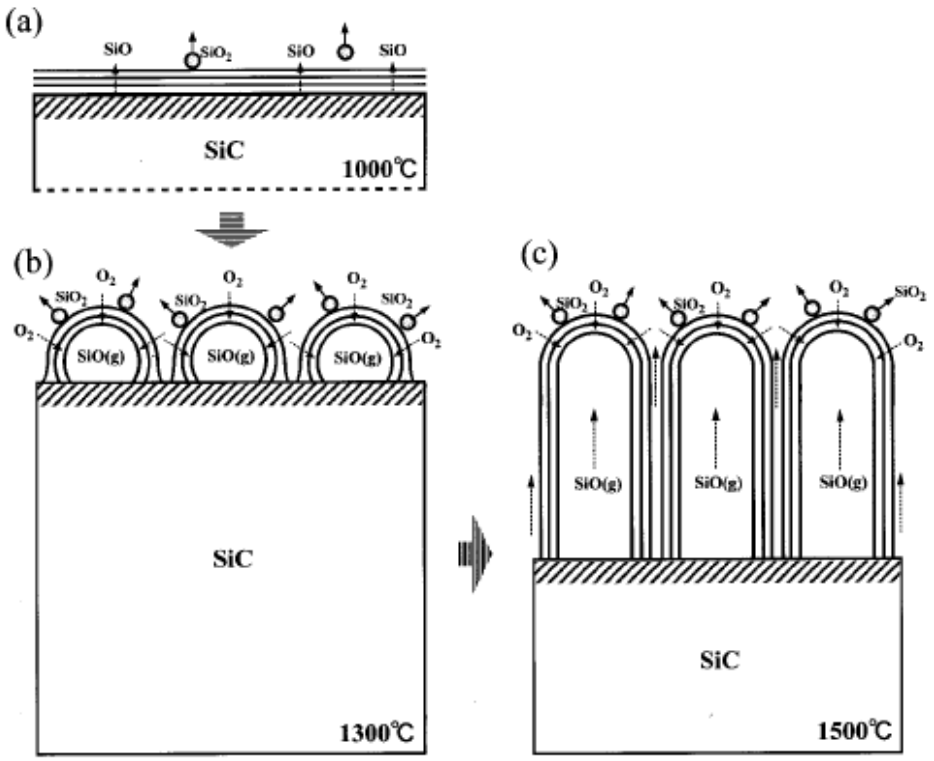

Fig. 43. Schematic diagram for the formation mechanism of the CNT film on the carbon terminated face of the SiC. (a) Above 1000^0 C, graphite sheets are formed parallel to the SiC substrate. (b) Around 1300^0 C, graphite nanocaps are generated on the surface by the SiO gas bubbles. The graphite sheet curves outward on the SiC (0001) plane. (c) CNT grow towards the interior of the SiC wafer, as the Si atoms evaporate [23].

The size of the nanocaps is determined by the pressure of the SiO gas. Once the nanocaps are formed, the graphite starts to become perpendicular to the plane of the SiC wafer. It is suggested that the carbon atoms perpendicular to the plane have a σ-bond with the carbon atoms in the plane of the SiC. The σ-bond is stronger and more stable than a π-bond and is preferentially preserved allowing the graphite sheets to grow into nanotubes, with a diameter given by the size of the nanocaps.

There are two types of nanocaps formed on the surface: spherical particles of amorphous carbon and graphite fragments as shown in Fig. 44. At high annealing temperature, the spherical caps are converted to graphite, whereas the two to four layered graphite fragments, are generated when there is a change in the height of the substrate. At

the edges, where there is a change in height, the π electronic states are active and the graphite sheets tend to connect the carbon atoms together on the surface.

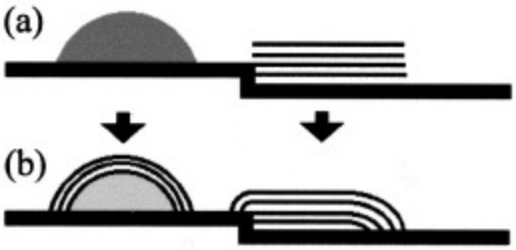

Fig. 44. The formation of the carbon nanocaps on the surface of the carbon terminated face of SiC. (a) The formation of amorphous carbon clusters and graphite layers on the surface. (b) The formation of two types of carbon nanocaps [24].

However, on the Si-face, Kusunoki et al.,[24] observed graphite sheets growing parallel to the substrate (Fig. 45). No carbon nanocaps were formed on the surface which would have resulted in the formation of CNT. As the silicon atoms in the top layer evaporate, it leaves behind the carbon atoms which are attached to the silicon atoms in the third layer by vertical bonding. The carbon atoms remain in their initial position, without forming nanocaps. As silicon atoms from the inner layers are evaporated, a dense graphite sheet is formed and the lowermost carbon atoms are still bonded to the silicon atoms. The thick parallel sheets inhibit the formation of the nanocaps.

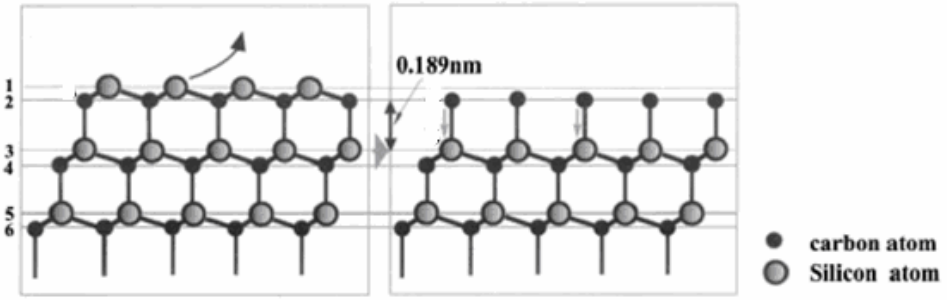

Fig. 45. The evaporation of the silicon atoms from substrate [26].

The difference between the growth mechanism on the Si-face and the C-face could also be explained in terms of the surface energies [24]. The growth pattern is affected by the relation between the surface energy of the adsorbed material γ_A and that of the substrate γ_B. If γ_A is greater than γ_B, then nucleated clusters are generated and if γ_A is less or equal to γ_B, monatomic layers are formed. We can therefore conclude that $\gamma_{Si\text{-}face} > \gamma_G > \gamma_{C\text{-}face}$ where $\gamma_{Si\text{-}face}$, $\gamma_{C\text{-}face}$ and γ_G are the surface energy of the Si-face and C-face of the silicon carbide and the graphite (0001) plane, respectively.

Watanabe et al., [27] studied the parameters which affect the growth of the CNT and how they are related to the growth process and the initial growth mechanism. The study was carried out using an in situ high resolution transmission electron microscope, which can sustain a temperature higher than 1300^o C. The β-SiC (111), which has a cubic lattice was heated for 30 minutes at 1080^o C, 1170^o C and 1360^o C and the diffraction images were observed at the nanometer scale. No change in the image contrast was observed from room temperature to a temperature of 1080^o C, i.e., the diffraction image stayed the same. As the temperature was increased to 1170^o C, a change in the contrast of diffraction image was seen. Watanabe et al., attributed these contrasts to the change in internal structure and local strains in the lattice of the SiC due to heating. As the temperature exceeded 1170^o C, the contrasts disappeared and this can be explained due to the evaporation of the silicon atoms. At 1360^o C, as more silicon atoms evaporate, thin layers of amorphous carbon can be seen at the edge of the sample. At higher temperature, graphitization of the amorphous carbon takes place and a thin layer of graphite was observed, which was oriented parallel to the surface. After heating for 30 min. at 1360^o C, white circles contrasts were observed in the diffraction image with diameters of 3 nm to 7 nm and a height profile ranging from 1.5 nm to 3 nm. It is therefore anticipated that the CNT are then formed by the lifting of the graphite (001) plane along the (111) direction. The caps of the CNT are formed by carbon atoms arranged in pentagons while heptagons of carbon atoms are formed in area where the diameter expands (Fig. 46 and Fig. 47). The formation of pentagons and heptagons occurs from graphene, which is essentially composed of hexagons. The nucleation of the pentagons at the edges of the open ends cause the CNT to incline inwards and cause closure of the CNT whereas the heptagons cause the CNT to curve outwards and aid in

the growth of the CNT. The formation mechanism of the pentagons and heptagons from the hexagons of graphene sheet is not fully understood.

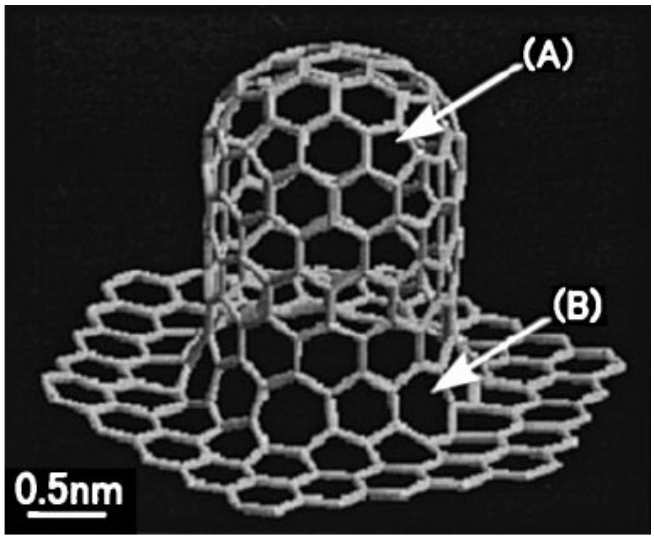

Fig. 46. Atomic model of a carbon nanotube formed by the lift of the graphene sheet. A pentagon is located at (A) near the cap of the nanotube, and a heptagon at the foot of the nanocap (B) [23].

At higher temperature, other graphite layers are formed and this leads to the formation of double-walled and multi-walled CNT [27].

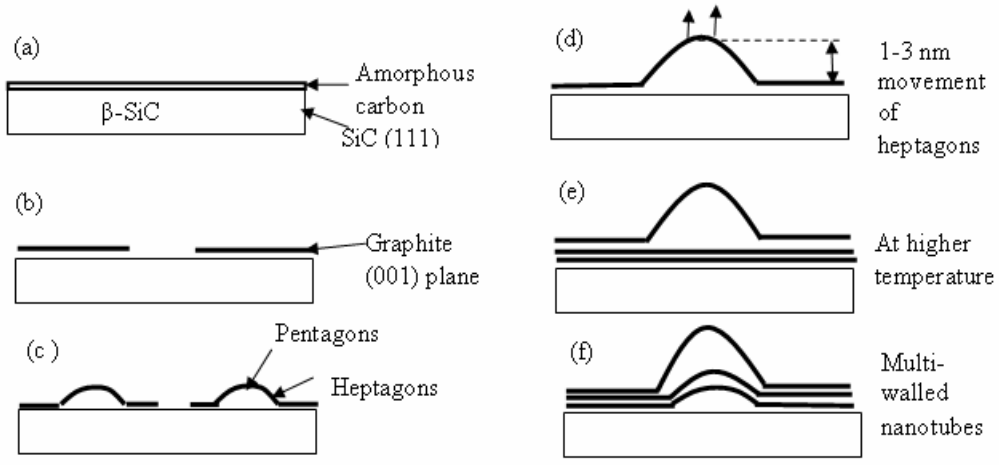

Fig. 47. A schematic illustration of the initial growth process of the CNT in a cross sectional view. (a) Formation of amorphous carbon on the SiC substrate at a temperature of 1360^{o} C. (b) Amorphous carbon is graphitized into thin graphite sheets in a direction parallel to the surface. (c) CNT are formed by the lift of part of the graphite sheet along the (111) direction by a generation of pentagons and heptagons in the graphene. (d) CNT grow by the movement of the heptagons in the opposite direction against the growth direction. (e) At higher temperature, other graphite layers are formed below the nanotubes. (f) Double- and multi-walled nanotubes are formed by the lifting of the graphite sheets [27].

Nagano et al., [25] was able to observe the growth of CNT on the silicon terminated face of the sample and confirmed that the presence of the silicon oxide on the wafer affects the growth mechanism. The silicon carbide substrates were soaked in 10% hydrofluoric acid for 0.5 hours to remove the oxide on the surface of the substrate and the samples were then rinsed in deionized water. Some of the samples were not soaked in the acid, so as to compare the growth mechanism. The samples were then heated in a furnace at 1773^{o} C for 2 hrs. at a pressure of 10^{-4} Torr. Carbon nanotubes were formed perpendicular to both the Si (0001) and C (0001) faces of the samples treated with hydrofluoric acid. However, in the samples that were not treated with hydrofluoric acid, carbon nanotubes and graphite were formed on the C (0001) and Si (0001) terminated face, respectively. Hence, it was deduced that the presence of the SiO_2 on the Si-face prevented the formation of the CNT.

More recent studies have shown that thermally stable oxygen-carbon compounds are involved in the growth process [28]. A multilayer structural model of CNT/silicon

carbide structure is suggested, based on spectroscopic ellipsometry measurements at the CNT/silicon carbide structures grown at various temperatures and pressures. Ellipsometry is a fast, sensitive and non-destructive method for thin films and nanostructural characterizations. It is an excellent technique for investigation of interfacial structures as the vertical resolution is 1 nm and with an appropriate model, the thickness of the different layers can be obtained.

4H-SiC with a nitrogen doping concentration of 5.3×10^{17} cm^{-3} were used in this experiment. The samples were cleaned by a modified RCA method as follows: (a) NH_4OH: H_2O_2:H_2O (1:1:2) at 85^0 C for 5 min., (b) HCl:H_2O_2:H_2O (1:1:2) at 85^0 C for 5 min., (c) HF:H_2O (20 % solution) for 5 min., (d) HNO_3 (50 % solution) at 90^0 C for 5 min. and (e) HF:H_2O (10% solution) for 2 min. The samples were washed in deionized water between each step. The CNT were grown at a temperature between 1400^0 C to 1700^0 C and a pressure range of 10^{-3} to 10^{-5} Torr. The growth time was 30 to 120 min. The new model proposed by Boeckl et al.,[28] is a 5-layered structure as shown in Fig. 48.

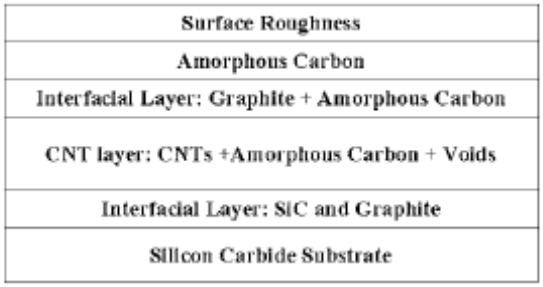

Fig. 48. Schematic representation of the five layer model for the CNT/silicon carbide structure [28].

The model includes a porous SiC layer, a graphite layer with voids, an interfacial layer between the silicon carbide substrate and the CNT. This layer acts as the structural transition between the CNT and the silicon carbide. Another interfacial layer with amorphous carbon and graphite components between the CNT layer and the amorphous carbon layer is also found. The main layer is the CNT layer which contains mainly CNT, voids and some amorphous carbon [28].

From the experiment, it was found that samples, grown at a pressure of 10^{-5} Torr at various temperatures, have a CNT layer which consists of 30 %-50 % CNT, 35 %- 60 % voids and 50 %-12 % of amorphous carbon in volume as shown in Fig. 49.

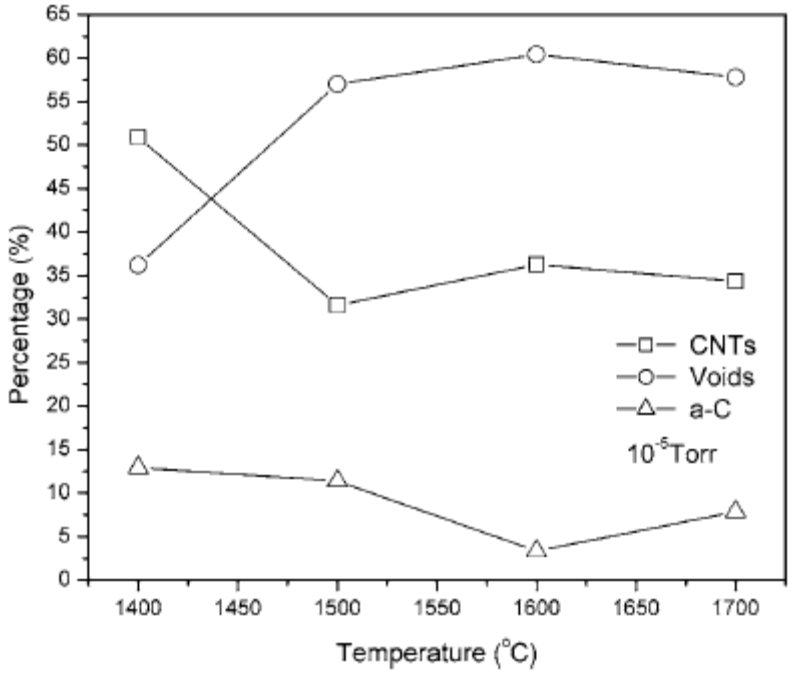

Fig. 49.Volume percentage of CNT, voids and amorphous carbon in the CNT layer at a pressure of 10^{-5} Torr for 30 min. at various temperatures [28].

As the temperature increases, the void content increases while the CNT/void ratio remains the same. It is also observed that the amorphous carbon in the CNT layer decreases as the temperature increases.

Similar analysis was performed for the samples prepared from 1400^{o} C to 1700^{o} C and pressures of 10^{-3} and 10^{-7} Torr. Fig. 50 shows that the CNT layer from the samples grown at 10^{-3} Torr at various temperatures consists of 30 %- 40 % of CNT, 50 %-70 % voids and less than 10 % of amorphous carbon in volume.

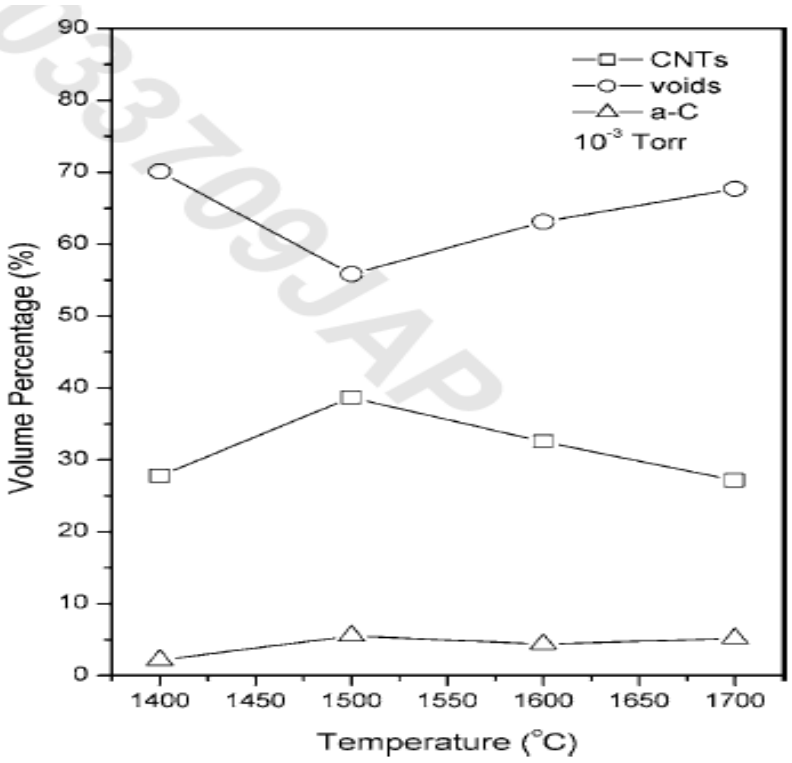

Fig. 50. The volume percentages of CNT, voids and amorphous carbon in the CNT layer at a pressure of 10^{-3} Torr for 30 min. at various temperatures [28].

However, at a pressure of 10^{-7} Torr and a temperature in the range of 1400^{o} C to 1500^{o} C, the thickness of CNT is only 2 to 4 nm, in which 92 % is amorphous carbon indicating that very few CNT are formed. It can therefore be deduced that the presence of oxygen is important for the growth of CNT from the silicon carbide decomposition process. Fig. 50 shows that at a given growth pressure, increasing the temperature leads to an increase in the CNT growth rate up to 1700^{o} C. The growth rate increases with increasing pressure at lower temperature (1400^{o} C to 1500^{o} C) and at higher temperature (1700^{o} C) the pressure has a negligible effect on the CNT thickness.

CHAPTER 6

ELECTROMAGNETIC CHARACTERIZATION OF CNT FILMS

6.1 Derivation of the resonant frequency and quality factor shifts when the tip touches the sample

The relative shift in frequency when the tip touches the sample will be derived from Eq.(30) in Chap. 3 and is shown again for convenience

$$\left(\frac{\Delta f}{f_0}\right)_{total} = \left(\frac{\Delta f}{f_0}\right)_1 + \left(\frac{\Delta f}{f_0}\right)_2 = -A\sum_{n=1}^{\infty} t_n \left[1 - \frac{1}{2}(1-b)\frac{1}{a_1^{'} + a_n^{'}}\right].$$

When the tip touches the sample, the following equations are obtained from Eq.(27) and Eq.(28) [29]

$$a_n^{'} = 1/n$$
$$t_n = b^{n-1}/n$$

Replacing it in Eq.(27) and after the performing the summation, the relative shift in frequency can be rewritten as

$$\left(\frac{\Delta f}{f_0}\right)_{total} = -A\sum_{n=1}^{\infty} \frac{b^{n-1}}{n}\left(1 - \frac{1}{2}(1-b)\left(\frac{n}{n+1}\right)\right)$$

$$= A\left(\frac{\ln(1-b)}{b} - \frac{(1-b)}{2b} - \frac{(1-b)}{2b^2}\ln(1-b)\right) \tag{34}$$

Expressing

$$\ln(1-b) = -\sum_{k=1}^{\infty}\left(\frac{b^k}{k}\right)$$

and

$$b = R\exp(i\varphi),$$

where

$$R = \left(\left(\varepsilon'^2 + \varepsilon''^2 - \varepsilon_0^2\right)^2 + 4\varepsilon''^2\varepsilon_0^2\right)^{1/2} \Big/ \left(\left(\varepsilon' + \varepsilon_0\right)^2 + \varepsilon''^2\right) \text{ and}$$

$$\varphi = \tan^{-1}\left(2\varepsilon''\varepsilon_0 \Big/ \left(\varepsilon'^2 + \varepsilon''^2 - \varepsilon_0^2\right)\right)$$

we have from Eq.(34)

$$\left(\frac{\Delta f}{f_0}\right)_{total} = \frac{A}{2}\left(1 - \frac{1}{b} + \sum_{k=1}^{\infty}\frac{1}{k}(b^{k-2} - 3b^{k-1})\right)$$

$$\left(\frac{\Delta f}{f_0}\right)_{total} = \left(\frac{\Delta f}{f_0}\right)_{real} + \left(\frac{\Delta f}{f_0}\right)_{imaginary}$$

$$= \frac{A}{2}\left(1 - \frac{\cos\varphi}{R} + \sum_{k=1}^{\infty}\frac{1}{k}\left(R^{k-2}\cos((k-2)\varphi\right) - 3R^{k-1}\cos((k-1)\varphi\right)$$

$$+ \frac{iA}{2}\left(\frac{\sin\varphi}{R} + \sum_{k=1}^{\infty}\frac{1}{k}\left(R^{k-2}\sin((k-2)\varphi) - 3R^{k-1}\sin((k-1)\varphi)\right)\right)$$

The change in the quality factor when tip touches the sample is given by [30]

$$\Delta\left(\frac{1}{Q}\right) = \frac{1}{Q} - \frac{1}{Q_0} = -(B + \tan\delta)\frac{\Delta f}{f_0}$$

where B is a constant determined experimentally (2.06×10^{-6}) and $\tan\delta = \varepsilon''/\varepsilon'$.

$$\left(\frac{\Delta f}{f_0}\right)_{real} = \frac{A}{2}\left(1 - \frac{\cos\varphi}{R} + \sum_{k=1}^{\infty}\frac{1}{k}\left(R^{k-2}\cos\left((k-2)\varphi\right) - 3R^{k-1}\cos\left((k-1)\varphi\right)\right)\right) \qquad (35)$$

$$\Delta\left(\frac{1}{Q}\right)_{real} = -\left(B + \frac{\varepsilon''}{\varepsilon'}\right)\left(\frac{\Delta f}{f_0}\right)_{real} \tag{36}$$

6.2 Experimental data for the resonant frequency and the Q-factor of the treated and untreated CNT samples

Graphs of the typical experimental values of the resonant frequency and the reciprocal of the Q-factor as a function of distance between the tip and the sample for the untreated and treated Si-face (3 hrs.) CNT films are plotted in Fig. 51, Fig. 52, Fig. 53 and Fig. 54, respectively. The quality factor is defined as the ratio $\omega_o/(\Delta\,\omega)$, where ω_o is the resonant frequency and $(\Delta\,\omega)$ is the full width at half maximum of the resonant frequency. The Q-factor is given by $(L/R^2C)^{1/2}$ where L is the inductance, R is the resistance and C is the capacitance of the sample coupled with the system. If the tip maintains constant height above the sample, the Q-factor will change according to local variation in resistance of the sample. The annealing time for the treated CNT sample was 40 min. under oxygen flow. This particular treatment time was chosen because this sample demonstrates a maximum improvement in surface conductivity in comparison to CNT samples treated for 25 min. and 60 min.

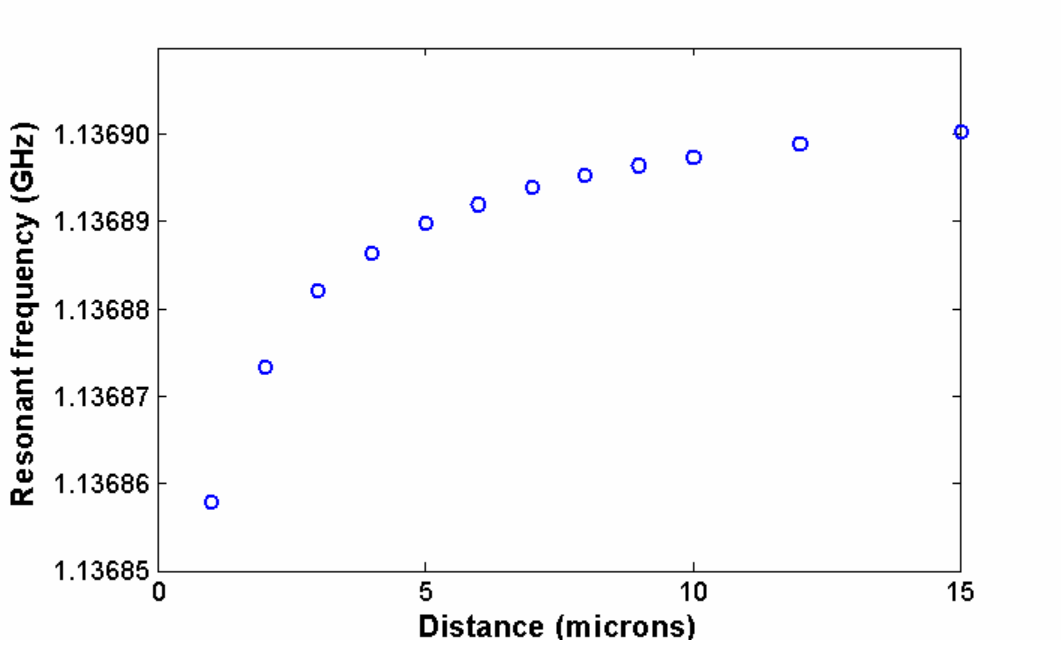

Fig. 51. Experimental data of resonant frequency for the untreated Si-face(3 hrs.) CNT film.

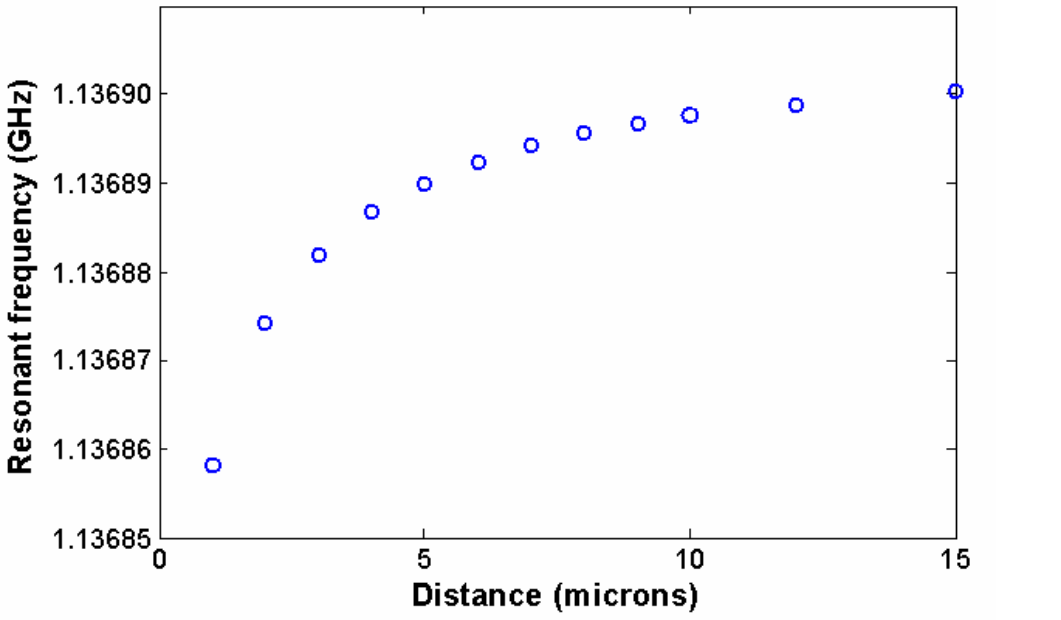

Fig. 52. Experimental data of resonant frequency for treated Si-face (3 hrs.) CNT film after 40 min. of annealing.

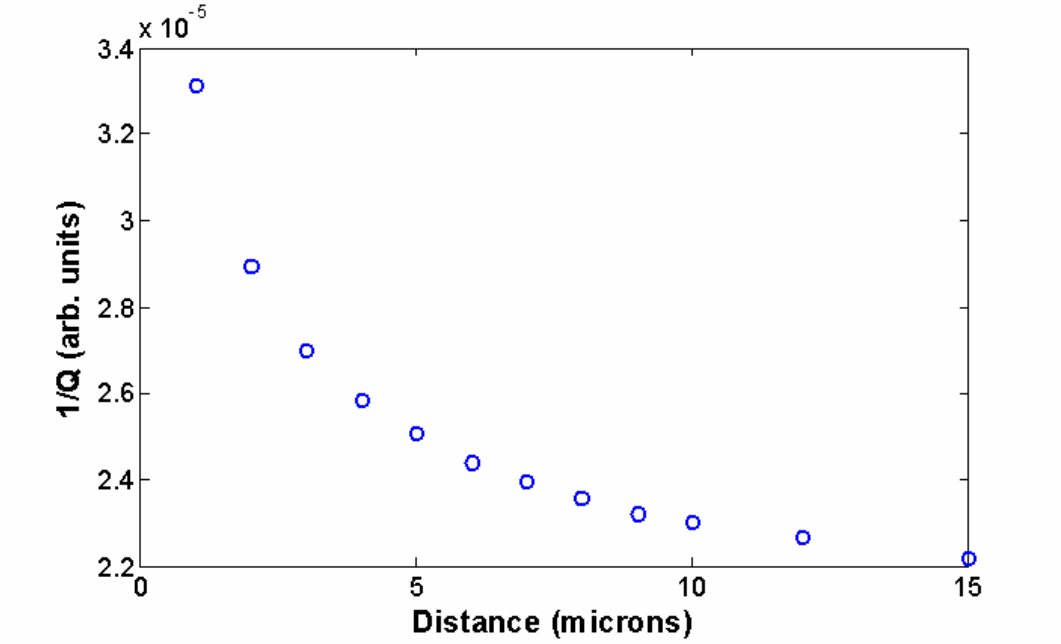

Fig. 53. Experimental data of the reciprocal Q-factor for the untreated Si-face(3 hrs.) CNT film.

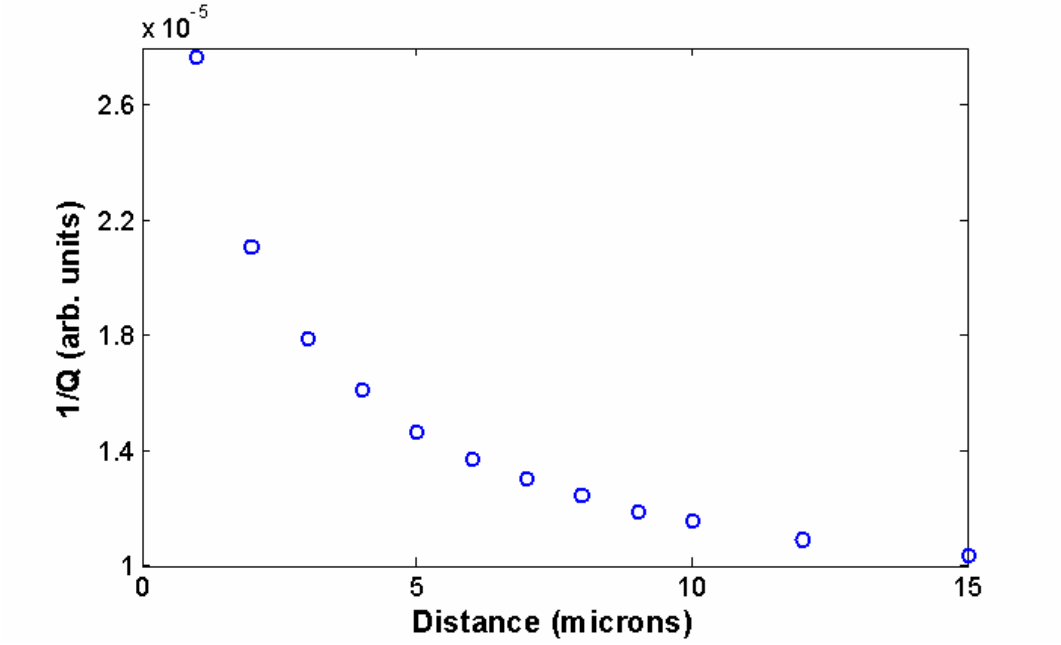

Fig. 54. Experimental data of the reciprocal Q-factor for the treated Si-face (3 hrs.) CNT film after 40 min. of annealing.

An indication of surface conductivity (Q-factor) was also measured at a frequency of 1 GHz in an area of 1 mm × 1 mm chosen arbitrarily before treatment but same area is measured after treatment of the CNT samples. The average value of the Q-factor was calculated in chosen area for each sample in addition to the values of Q-factor specified for 3 particular locations and compared at the same geometrical locations with the other CNT samples annealed for 25 min., 40 min. and 60 min., respectively.

CHAPTER 7

RESULTS AND DISCUSSION

The main goal of my thesis is to study the conductive properties of CNT films fabricated by the surface decomposition of silicon carbide and how these properties can be enhanced when the films are subjected to the annealing process causing uncapping of the CNT. According to existing experimental works, there are indications that uncapping of the CNT provides substantial increase of these properties [17]. The uncapping of the tubes is better for field-emission because the relative tip size gets smaller because the emission points are located around the opened edge walls of the tube rather than the dome of the closed CNT. The major interest in this area is related to field emission applications of the CNT films. Several CNT samples grown at different conditions and treated to increase their conductive properties were listed and specified in Tab.III and Tab. IV, respectively. There are two available techniques to measure the electrical properties of the CNT films, namely, by direct measurement of field-emission from the samples or by local permittivity measurements related to conductive properties of the samples using evanescent microwave microscope. With intention to perform later direct field-emission measurements such as the current density, turn-on field and the threshold field for our samples, I have decided initially to concentrate on preliminary studies of the conductive properties of the CNT films by using evanescent microwave microscopy due to the unavailability of the field-emission equipment. But whatever I will conclude here, it should be useful for future work on the field-emission of the CNT films.

7.1 Structural and chemical characterization of CNT films

The main objective of this study was to anneal the CNT films at 400^0 C in the presence of oxygen or carbon dioxide with optimized ramping conditions in order to uncap the single- and multi-walled carbon nanotubes. Although the study was performed on several CNT samples listed in Tab.III and Tab. IV, I will restrict my experimental and theoretical results and discussion only to the most typical ones. The uncapping of the carbon nanotubes were clearly seen in our SEM and AFM images and typical examples of uncapping are demonstrated in Fig. 55 and Fig. 56 for the CNT film on Si-face (3

hrs.). The top view SEM images of the CNT films on the Si-face (3 hrs.) were taken before and after 40 and 60 minutes intervals of annealing time. These films were treated with oxygen during annealing at 400^{o} C and cooling from 400^{o} C to 100^{o} C, before removal of them from the box furnace.

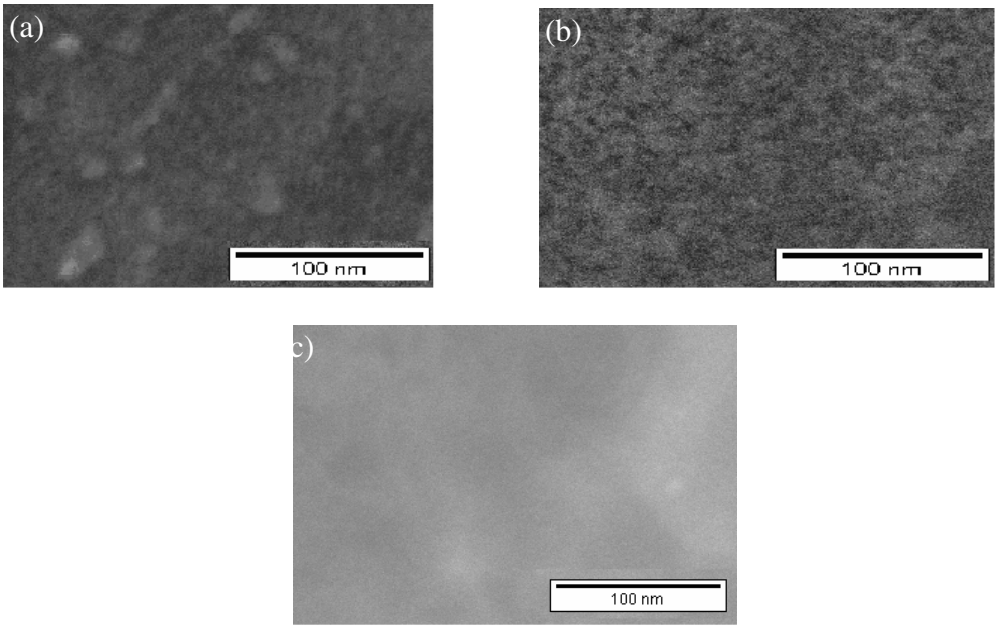

Fig. 55. SEM image for untreated CNT film (a), for treated 40 min.(b) and treated for 60 min.(c).

The SEM images indicate the presence of white patches on the surface for the untreated film (Fig. 55(a)). The white spots are due to the presence of (this may be amorphous) graphitic carbon (see Fig. 25) formed on the surface of the film during the decomposition of silicon carbide (Fig. 16) as the temperature increases and is also due to the adsorbed oxygen when the film is removed from the furnace. In addition to this, the hexagonal structure of CNT array can be seen in other locations of the surface. The SEM image of the film (Fig. 55(b)) after treatment for 40 min. shows black patches more likely indicating that the CNT have been uncapped. Further treatment is causing complete removal of the CNT and is depicted in (Fig. 55(c)), which was treated for 60 min. in oxygen and does not have any significant features.

AFM images of the same CNT film confirm our SEM observations. The white patches in Fig. 56(a) can also be interpreted as coalesced carbon nanotubes grown on silicon carbide single grain. Fig. 56(b) clearly shows partial uncapping of the carbon nanotubes on the sample after 25 min. of treatment, while Fig. 56(c) represents SiC grains without any noticeable presence of carbon nanotubes.

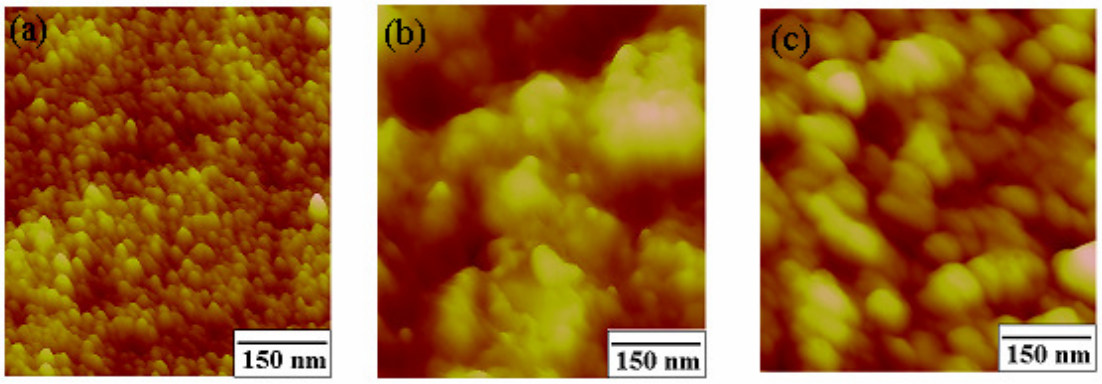

Fig. 56. AFM image for untreated CNT film (a), for treated 25 min.(b) and treated for 60 min.(c).

Our EDS chemical analysis was restricted to untreated CNT films. Typical SEM/EDS spectra in Fig. 35, Fig. 36 and Fig. 37 confirm gradual decrease of silicon in the CNT films for C-face (1 hr.), C-face (3 hrs.) and C-face (6 hrs.) due to chemical reaction (Eq.31) describing the selective removal of silicon atoms from the silicon carbide substrate (see Fig. 42 and Fig. 45). It was also confirmed in the plots in Fig. 38, Fig. 39 and Fig. 40 which represent peak intensities as a function of growth time. Typical qualitative TEM/EDS spectra in Fig. 33 and the quantitative summary in Tab.V confirm evaporation of silicon from the silicon carbide substrate. There should be no significant variation in the EDS spectra after annealing.

Typical XRD patterns of untreated CNT films for C-face (1 hr.) and C-face (6 hrs.) are plotted in Fig. 30, Fig. 31 and Fig. 32. The crystallinity of the CNT samples clearly decreases with increasing growth time as shown in Fig. 31 and Fig. 32. It also confirms evaporation of silicon atoms since the intensity of the silicon carbide peak decreases. In order to prove these results, our typical treated CNT film (C-face (6 hrs.)) was subjected to a maximum annealing time (60 min.) to remove crystalline carbon

nanotubes. The XRD pattern for this treated sample is shown in Fig. 57. The graph indicates a lack of crystallinity in this treated sample after the removal of crystalline carbon nanotubes. This observation is in agreement with the model proposed by Boeckl et al.,[28].

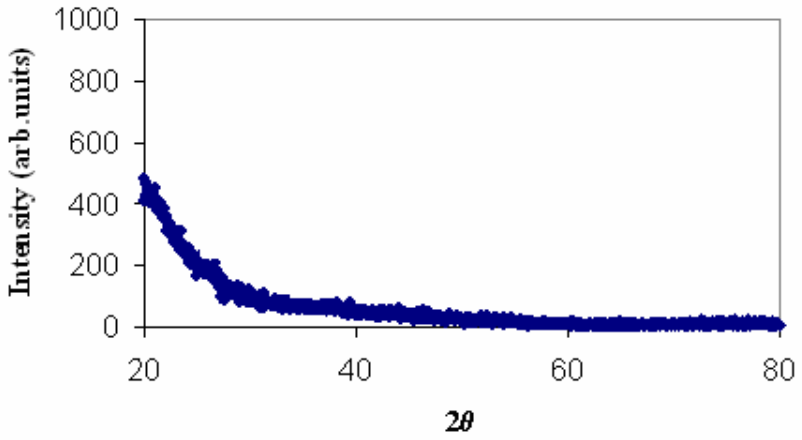

Fig. 57. XRD pattern for the CNT film on C-face (6 hrs.) after 60 min. of annealing under oxygen flow.

7.2 Electromagnetic characterization of carbon nanotube films by using evanescent microwave measurements

Theoretical model, describing a shift in the relative resonant frequency and in the reciprocal Q-factor (Eq.(30) and Eq.(31)) as a function of the tip-sample distance (from 15 μm to 1 μm), is used to describe experimental data taken for typical untreated and treated (40 min. in oxygen) Si-face (3 hrs.) CNT films (Fig. 51, Fig. 52, Fig. 53 and Fig. 54) by using evanescent microwave measurements at 1 GHz. The real and imaginary (conductive) component of permittivities of the above-mentioned samples calculated from theoretical fitting of experimental data at a frequency of 1 GHz are in close agreement with the experimental values available from the literature (see, Tab.VI and Fig. 58 and Fig. 59).

Tab.VI. Real and imaginary component of permittivities for the untreated and treated Si-face (3 hrs.) CNT samples [31].

Si-face (3 hrs.) CNT sample	ε' (model)	ε'' (model)	ε' (literature)	ε'' (literature)
Untreated	47.0	13.5	-	-
Treated (40 min.)	33.5	15.7	~ 25	~ 15

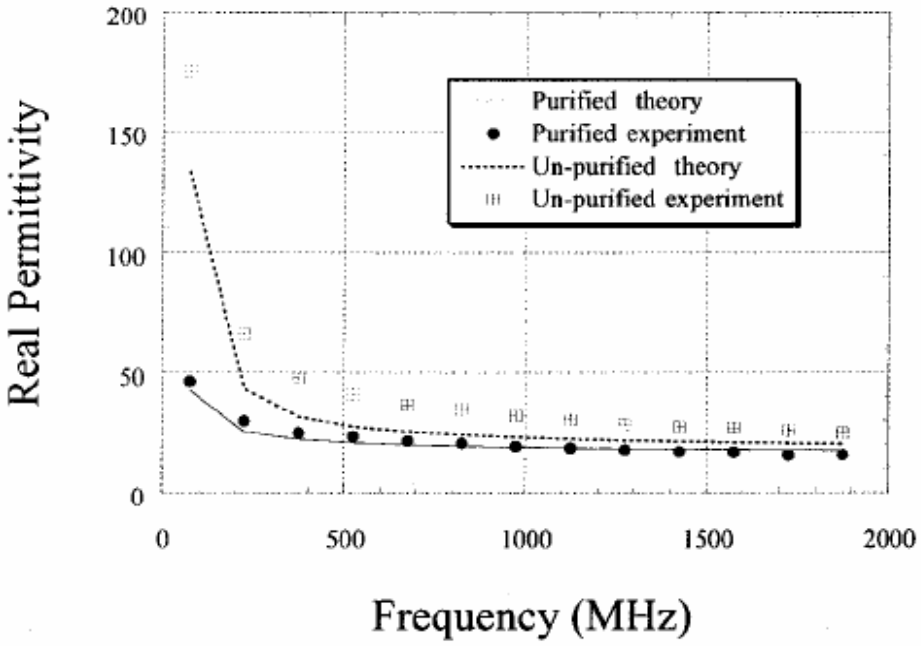

Fig. 58. Variation of the real permittivity of multi-walled CNT with frequency [31].

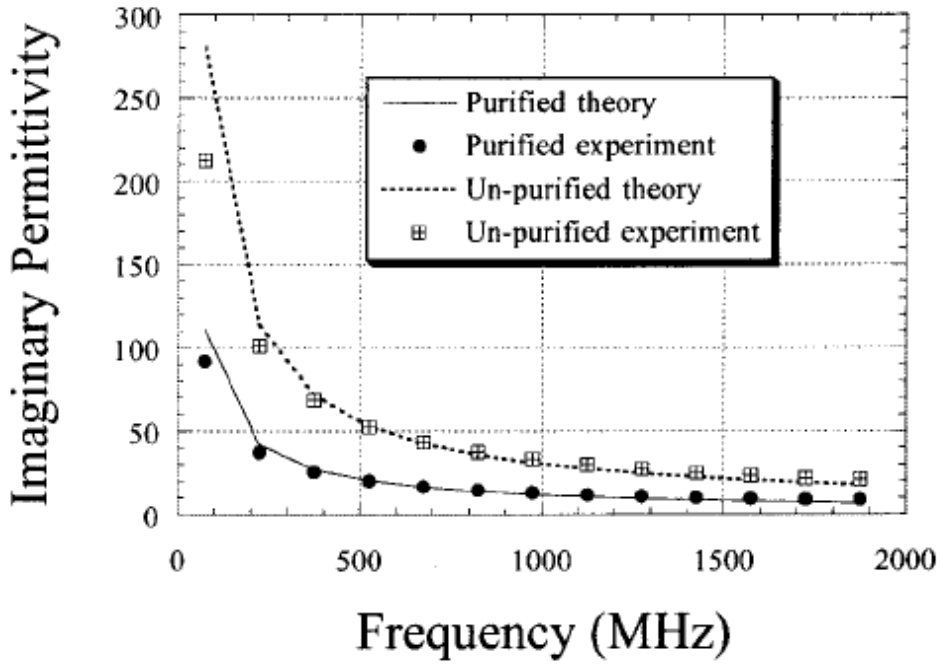

Fig. 59. Variation of the imaginary permittivity of multi-walled CNT with frequency [31].

Fig. 58 and Fig. 59 respectively show the variation of the real and imaginary component of permittivity of multi-walled CNT grown by CVD in the presence of Fe_3C which plays a role of the catalyst [31]. The catalyst particles were removed at the end of the synthesis process by high temperature annealing. The permittivity of the un-purified and purified CNT was them measured. The purified CNT real and imaginary components of permittivity at 1 GHz are in agreement with the values found in our study. The measurements of the real and imaginary component of permittivity for the untreated CNT are unique with no available reference in the literature.

There are other techniques available for determining the real and imaginary component of permittivity of materials such as ellipsometry. However, in this case, the evanescent microwave microscopy has been used because of its availability.

Our values of ε' obtained for the treated CNT films from the evanescent microwave measurements do not agree with values obtained for aligned semi-conducting single-walled CNT measured by combining absorption spectroscopy with transmission

ellipsometry and polarization dependent resonant Raman scattering [32]. The values of the real component of permittivity parallel and perpendicular to the single-walled nanotube symmetry axis are 7.5 and 1.6-1.7, respectively. However, the discrepancy of the values can be attributed to the fact that we have measured the permittivity of CNT films (both single-, multi- and coalesced multi-walled CNT) fabricated by surface decomposition of silicon carbide whereas Fagan and al.,[32] measured the permittivity of aligned single-walled CNT dispersed in a polymer film.

Comparing our theoretical model with experimental data (Fig. 51, Fig. 52, Fig. 53 and Fig. 54) for untreated and treated CNT samples, we generate the following plots (Fig. 60 and Fig. 61). Shift in resonant frequency as a function of distance for untreated and treated Si-face (3 hrs.) of CNT films shows a bigger shift for untreated sample. Based on our results (Tab.VI), untreated sample has a higher real component of permittivity, suggesting it is less conductive in comparison to treated sample [29]. Shift in the reciprocal of the Q-factor as a function of distance shown in Fig. 61 despite the fact that it is bigger for the treated CNT film follows physical reasoning that the reciprocal of the Q-factor is all the time greater for untreated sample than treated independently of the distance between the tip and the sample (Tab.VII).

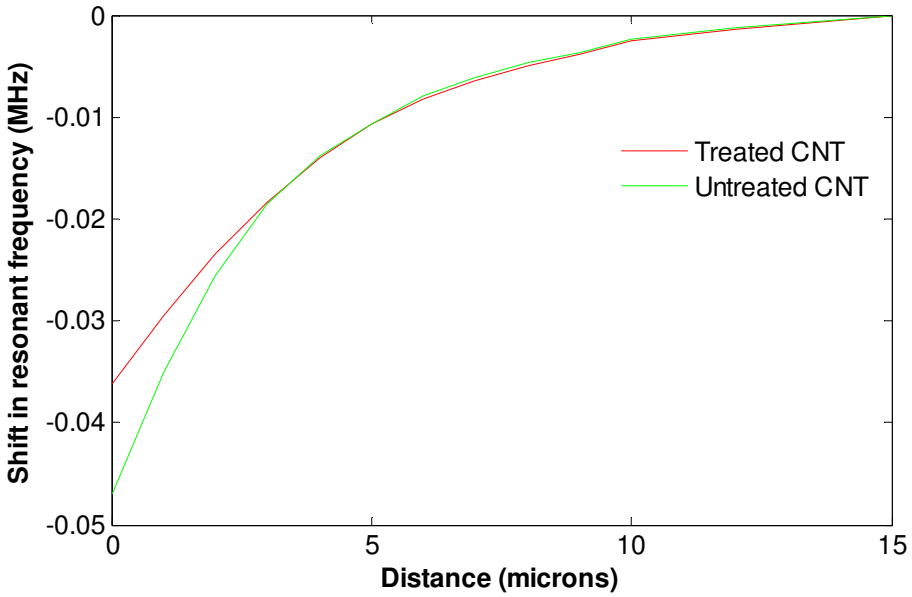

Fig. 60. Shift in resonant frequency as a function of distance for treated and untreated CNT sample.

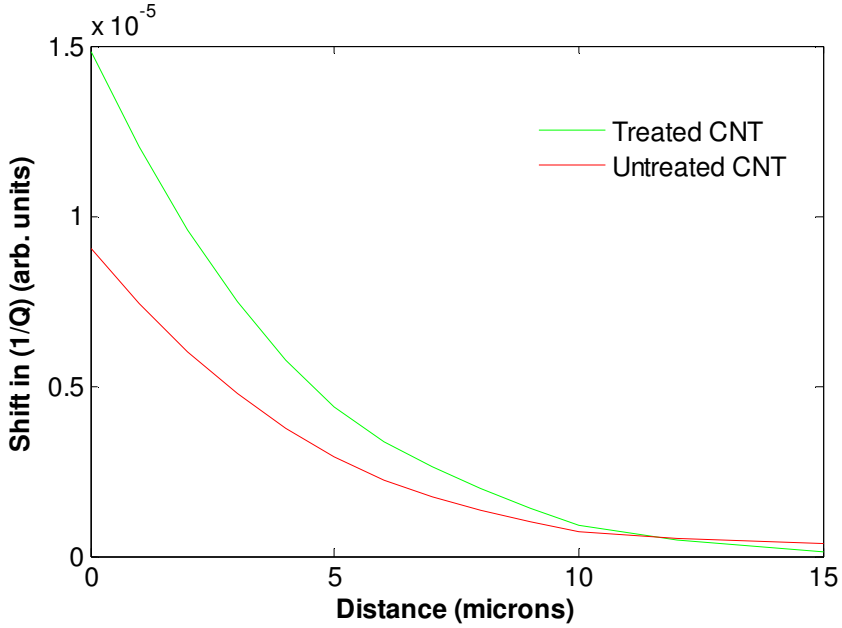

Fig. 61. Shift in the reciprocal of the Q-factor as a function of distance for the treated and untreated CNT sample.

Tab.VII. Comparison of the (1/Q)-factor for the treated and untreated CNT sample.

Si-face (3 hrs.) CNT samples	Distance (μm)	(1/Q)-factor (10^{-5} arb.units)
Untreated	1	3.31
	5	2.51
	10	2.30
Treated (40 min.)	1	2.78
	5	1.46
	10	1.16

This variation of Q-factor as a function of distance listed in Tab.VII can explain slight change in the imaginary part of permittivity (conductivity) for the treated sample (Tab.VI and Fig. 61) compared to untreated Si-face (3 hrs.) CNT film. This slight increase in conductivity is related to uncapping of the carbon nanotubes together with the removal of the graphitic layers of carbon and the adsorbed molecules on the surface of the sample.

7.3 Behavior of shift in resonant frequency and reciprocal of Q-factor when the tip touches the sample

Evanescent microwave microscopy measurements were done when the distance between tip and sample varied between 1 μm and 15 μm. Interesting questions arise what is the shift in the resonant frequency and the Q-factor when the tip is touching the sample (g = 0, Fig. 15). Usually that kind of measurements are avoided by experimentalists in order not to damage the tip of the probe during this measurement. From theoretical point of view, it will be interesting to predict the values of the frequency and Q-factor shifts when the gap between the tip and sample is zero. The Eq.(35) and Eq.(36) in Chap.6 describe exactly theoretically these shifts. By substituting the values of ε' and ε'' for the treated and untreated CNT from the Tab.VI into the Eq.(35) and Eq.(36) , the frequency shift at g = 0 was calculated by using Mathematica. The reference resonant frequency for the treated and untreated CNT films is 1.1369 GHz. From Eq.(35), the value of Δf found for k =1 to k = 100,000 iterations is found to be ─ 0.048MHz for the treated CNT film and ─ 0.0525 MHz for the untreated CNT film. The best smooth line was then drawn through the experimental data and the theoretical point using Matlab program.

The same procedure was repeated with Eq.(36) to find the shift in the reciprocal of the Q-factor at g = 0. This shift is equal to 17.5×10^{-5} and 10.8×10^{-5} for the treated and untreated CNT films, respectively.

The experimentally determined frequency shift is greater for the untreated CNT sample which is opposite to the shift in the reciprocal of its Q-factor. The theoretical model predicts the shift in the frequency and the reciprocal of the Q-factor correctly. The shift in the frequency is more sensitive to the value of ε' and since the untreated CNT sample has a greater ε', it results in more significant change in this shift. Finally, the shift in the reciprocal of the Q-factor is greater for the treated than untreated CNT sample since it is more sensitive to ε'' which is greater for treated.

It is more interesting to see if our model is suitable to predict theoretically existing experimental data [30] for resonant frequency shift at g = 0 of dielectric

materials such as for example MgO and LAO ($\varepsilon'' \approx 0$). Fig. 62. shows the experimental data for the change in resonant frequency as a function of the relative dielectric constant.

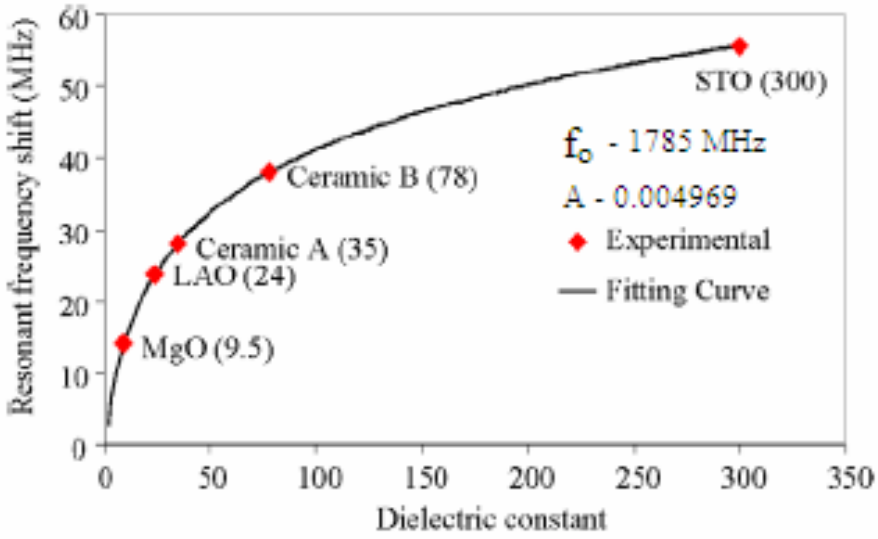

Fig. 62. Experimental data for the resonant frequency shift as a function of the dielectric constant [30].

Tab.VIII shows the value of the frequency shift calculated from our theoretical model (Eq.(35)). The value of A and f_o used in our calculations are 0.004969 and 1785 MHz, respectively.

Tab.VIII. Theoretical frequency shift calculated from our theoretical model.

Material	ε	Δf (MHz)
MgO	9.5	17.1
LAO	24	23.6

Our theoretical frequency shifts matches closely experimental data from Fig. 62.

7.4 X-Y scans of Q-factor of CNT films

The most important physical properties of the treated and untreated CNT samples are their local surface conductivity which has significant impact on their field emission. Q-factor mapping is performed in the area of 0.1 mm by 0.1 mm for the samples before

and after annealing treatment subjected to oxygen or carbon dioxide atmosphere. Fig. 63 and Fig. 64 show the Q-factor of the C-face (3 hrs.) before and after 25 min. of annealing under oxygen flow, respectively.

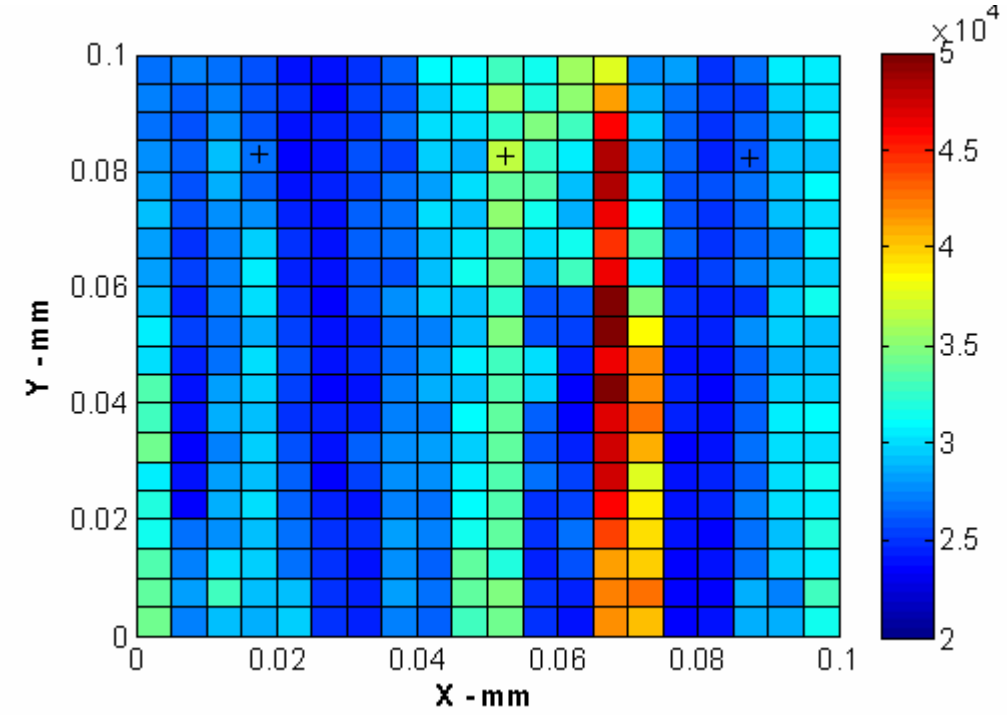

Fig. 63. Variation of the Q-factor for the untreated C-face (3 hrs.).

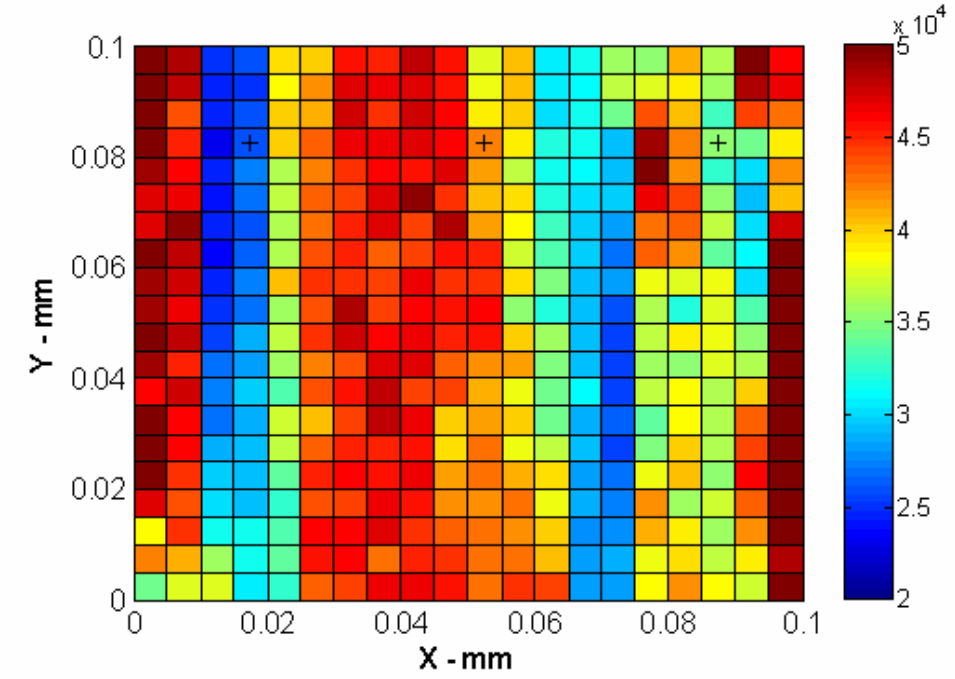

Fig. 64. Variation of the Q-factor for the C-face (3 hrs.) annealed 25 min. under oxygen flow.

The Q-factor for the C-face (3 hrs.) was measured at the locations indicated by a "+" on the diagram before and after treatment. Tab.IX summarizes the values obtained at these three specific locations.

Tab.IX. Q-factor values at the specific locations for the C-face (3 hrs.) CNT samples before and after treatment under oxygen flow.

Coordinates	(4,17)	(11,17)	(18,17)
Q-factor (untreated) (10^4 arb.units)	2.67	3.22	2.53
Q-factor (treated 25 min.) (10^4 arb.units)	3.10	3.77	3.56

The mean Q-factor over the area of 0.1 mm by 0.1 mm was calculated and the values are summarized in Tab.X.

Tab.X. Mean Q-factor values for the untreated and treated C-face (3 hrs.) CNT samples before and after treatment under oxygen flow.

Samples	Mean Q-factor (10^4 arb.units)
Untreated C-face (3 hrs.)	2.92
Treated C-face (3 hrs.) for 25 min. under O_2 flow	3.92

The experimental results shows that the conductivity improved by 35 % after annealing the sample for 25 min. under oxygen flow.

Fig. 65 and Fig. 66 show the Q-factor of the Si-face (3 hrs.) before and after 25 minutes of annealing under oxygen flow, respectively.

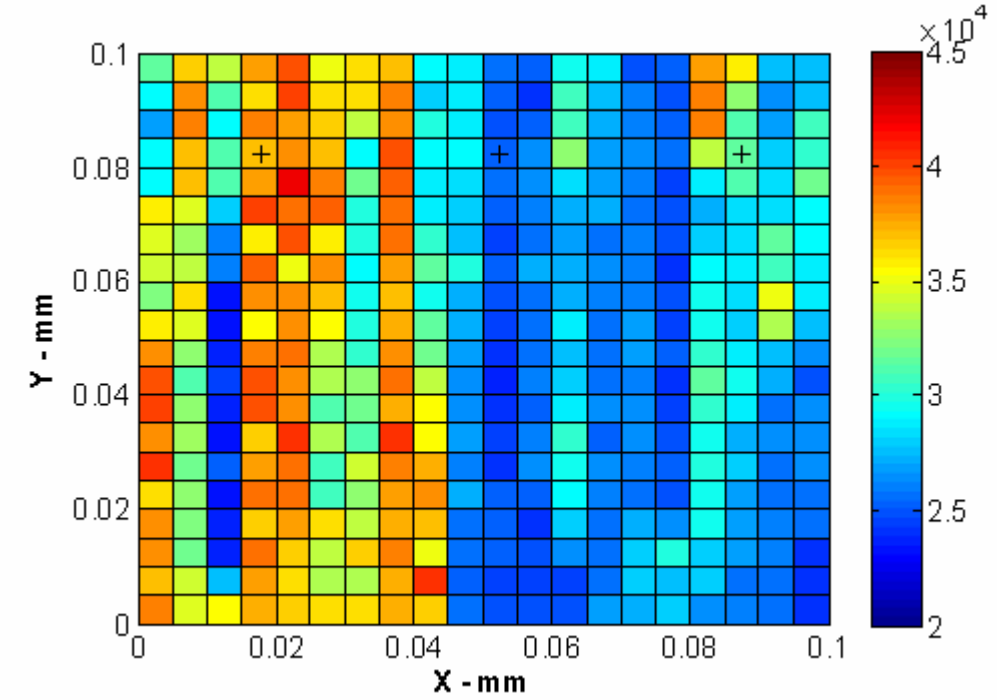

Fig. 65. Variation of the Q-factor for the untreated Si-face (3 hrs.).

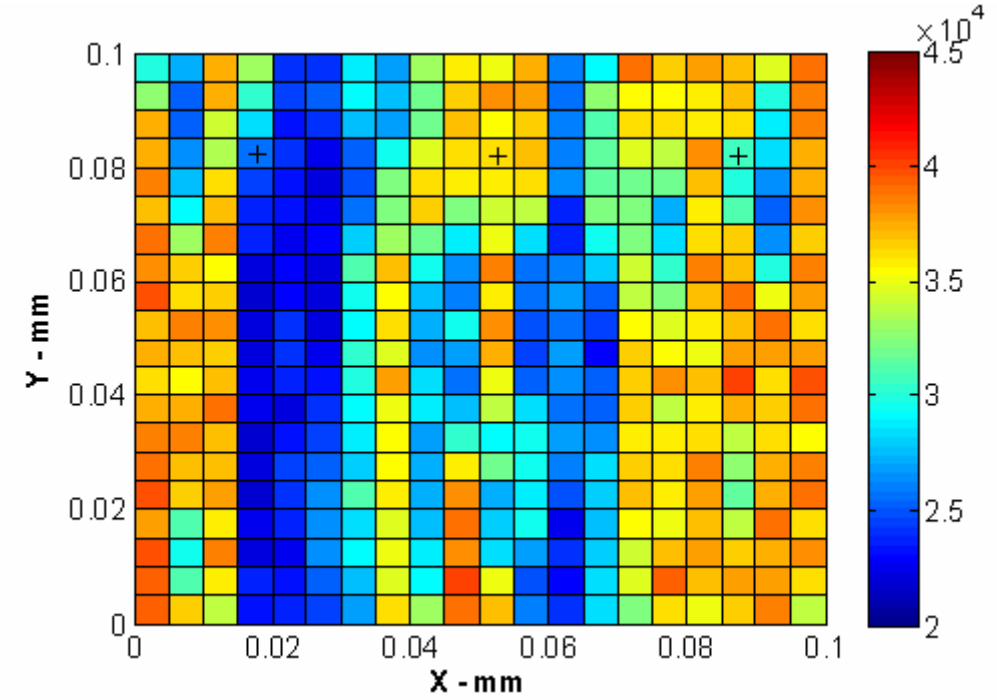

Fig. 66. Variation of the Q-factor for the Si-face (3 hrs.) annealed 25 min. under oxygen flow.

The Q-factor for the Si-face (3 hrs.) was measured at the locations indicated by a "+" on the diagram before and after treatment. Tab.XI summarizes the values obtained at these three specific locations.

Tab.XI. Q-factor values at specific locations of Si-face (3 hrs.) CNT samples before and after treatment under oxygen flow.

Coordinates	(4,17)	(11,17)	(18,17)
Q (untreated) (10^4 arb.units)	3.17	2.78	3.07
Q (treated 25 mins.) (10^4 arb.units)	2.29	3.71	3.13

The mean Q-factor over the area of 0.1 mm by 0.1 mm was calculated and the values are summarized in Tab.XII.

Tab.XII. Mean Q-factor values for the untreated and treated Si-face (3 hrs.) CNT samples.

Sample	Mean Q-factor (10^4 arb.units)
Untreated Si-face (3 hrs.)	3.03
Treated Si-face (3 hrs.) for 25 min. under O_2 flow	3.18

The overall surface conductivity of the sample increases by 5 %. The maximum increase in the conductivity is about 35 % at some specific locations on the sample. The difference in the conductivity is due to the presence of cracks in the original untreated sample. Upon annealing the cracks propagate and causes a decrease in the conductivity in that region, which lowers the mean values.

Fig. 67, Fig. 68 and Fig. 69 show the Q-factor on an area 0.1 mm by 0.1 mm on the Si-face (3 hrs.) sample before treatment, after 40 min. and 60 min. of annealing under oxygen flow, respectively.

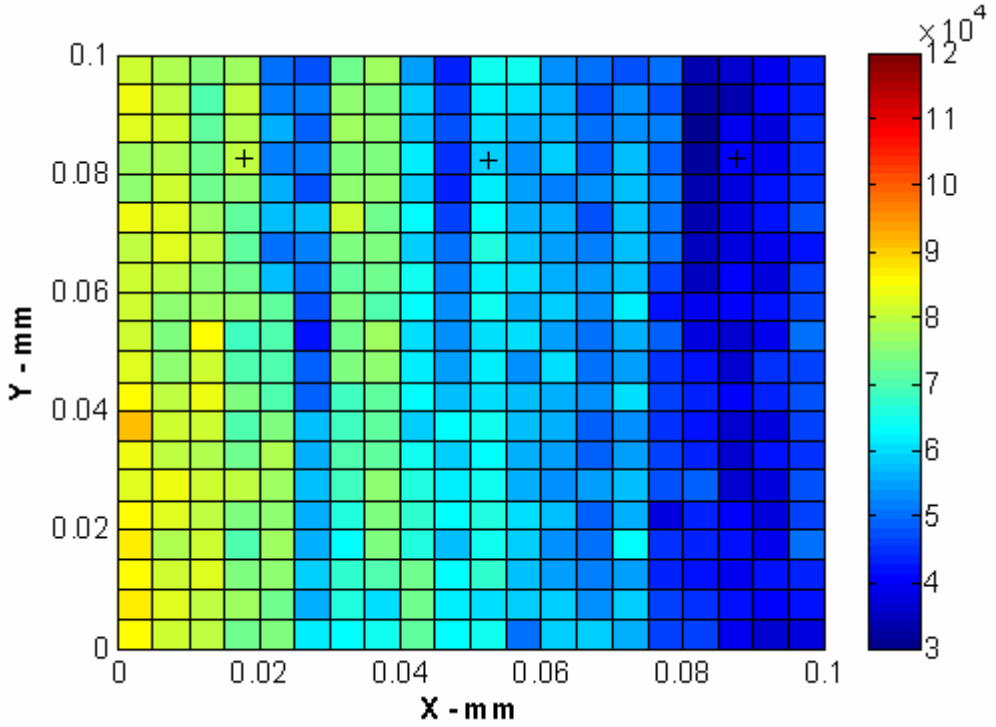

Fig. 67. Variation of the Q-factor for the untreated Si-face (3 hrs.).

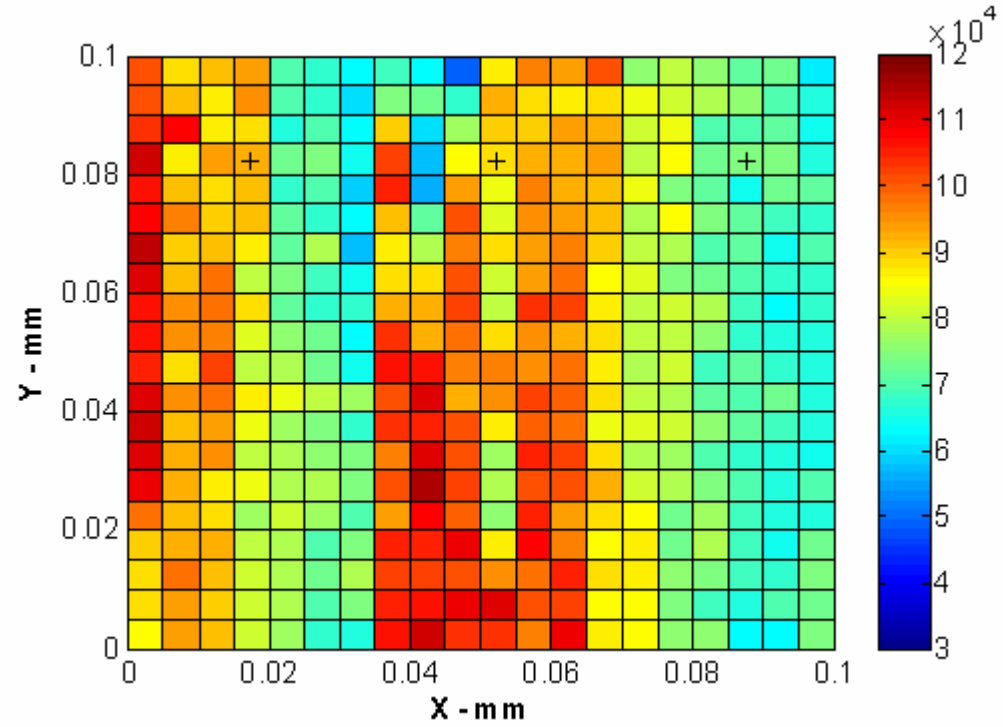

Fig. 68. Variation of the Q-factor for the Si-face (3 hrs.) annealed 40 min. under oxygen flow.

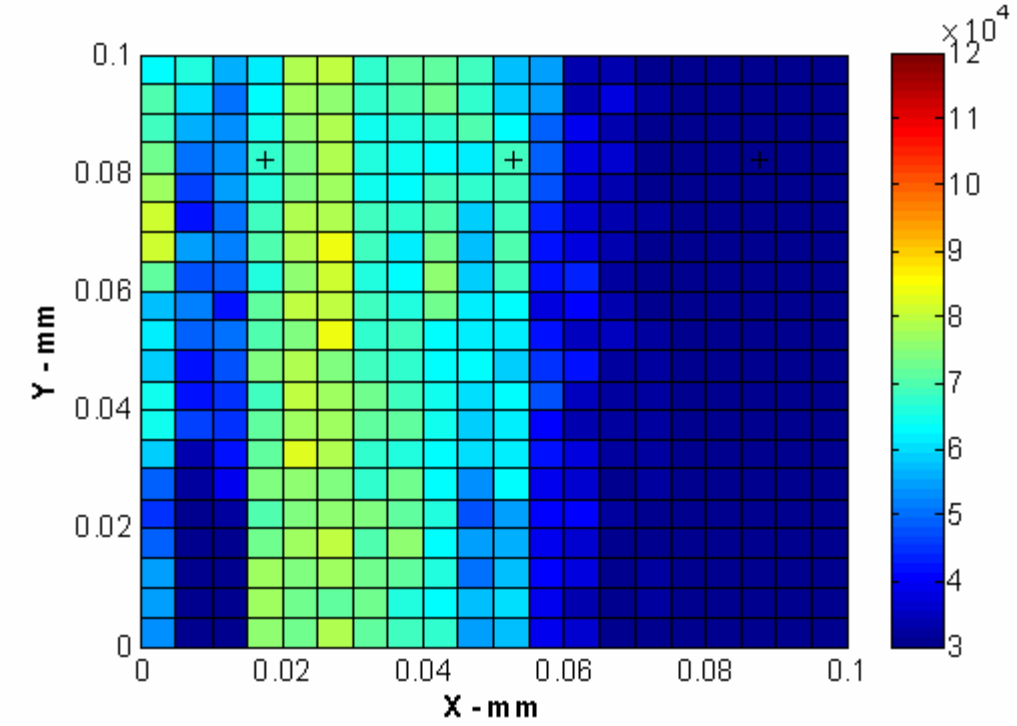

Fig. 69. Variation of the Q-factor for the Si-face (3 hrs.) annealed 60 min. under oxygen flow.

The Q-factor for the Si-face (3 hrs.) was measured at the locations indicated by a "+" on the diagram before and after treatment. Tab.XIII summarizes the values obtained at these three specific locations.

Tab.XIII. Q-factor values at specific locations of Si-face (3 hrs.) CNT samples before and after treatment under oxygen flow.

Coordinates	(4,17)	(11,17)	(18,17)
Q (untreated) (10^4 arb.units)	5.14	4.04	3.94
Q (treated 40 min.) (10^4 arb.units)	8.76	8.03	7.07
Q (treated 60 min.) (10^4 arb.units)	3.84	3.12	2.75

The mean Q-factor for each case was calculated and the values are summarized in Tab.XIV.

Tab.XIV. Mean Q-factor values for the untreated and treated Si-face (3 hrs.) CNT samples.

Samples	Mean Q-factor (10^4 arb.units)
Untreated Si-face (3 hrs.)	5.86
Treated Si-face (3 hrs.) for 40 min. under O_2 flow	8.31
Treated Si-face (3 hrs.) for 60 min. under O_2 flow	4.82

From the graphs (Fig. 67, Fig. 68 and Fig. 69) and the values recorded in Tab.XIII and Tab.XIV, it is clear that the mean Q-factor of the sample increases after 40 min. of annealing (Q-factor = 41.8 %). The reason is that annealing treatment uncaps the CNT in addition to the removal of the graphitic carbon layer and the adsorbed molecules on the surface of the sample. However, after 60 min. of annealing, there is a 41.9 % decrease in the Q-factor. This is because, after 60 min. of annealing, the CNT are completely burnt out and only amorphous carbon is left, which has a lower conductivity than the CNT (Fig. 57).

Fig. 70, Fig. 71, Fig. 72 and Fig. 73 show the Q-factor over the area of 0.1 mm by 0.1 mm on the Si-face (6 hrs.) sample before treatment, after 25 min., 40 min. and 60 min. of annealing under carbon dioxide flow, respectively.

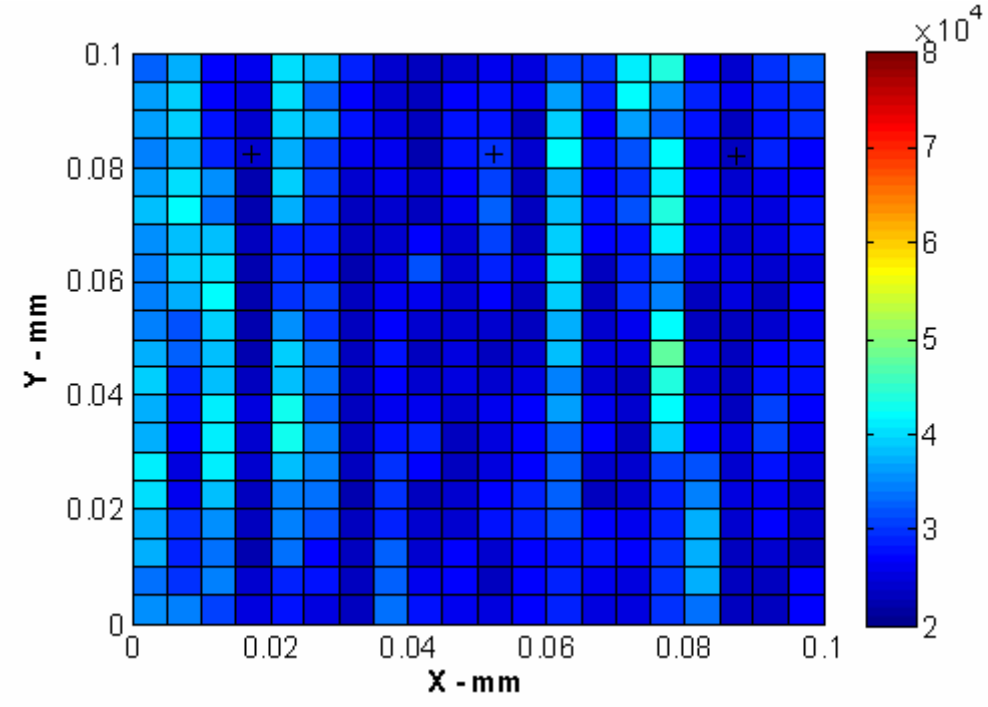

Fig. 70. Variation of the Q-factor for the untreated Si-face (6 hrs.).

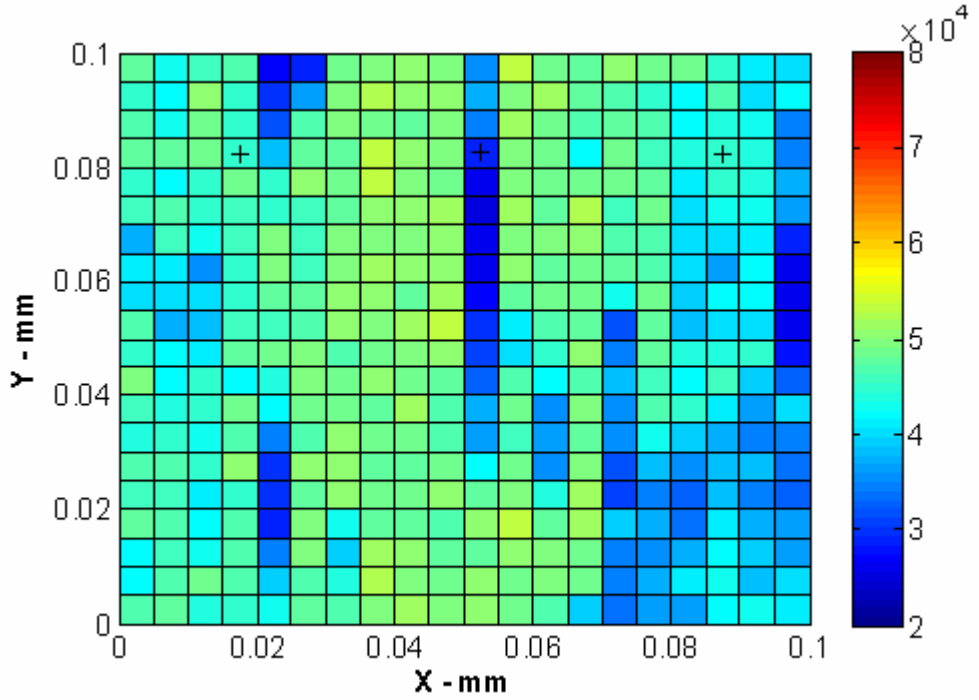

Fig. 71. Variation of the Q-factor for the Si-face (6 hrs.) annealed 25 min. under carbon dioxide flow.

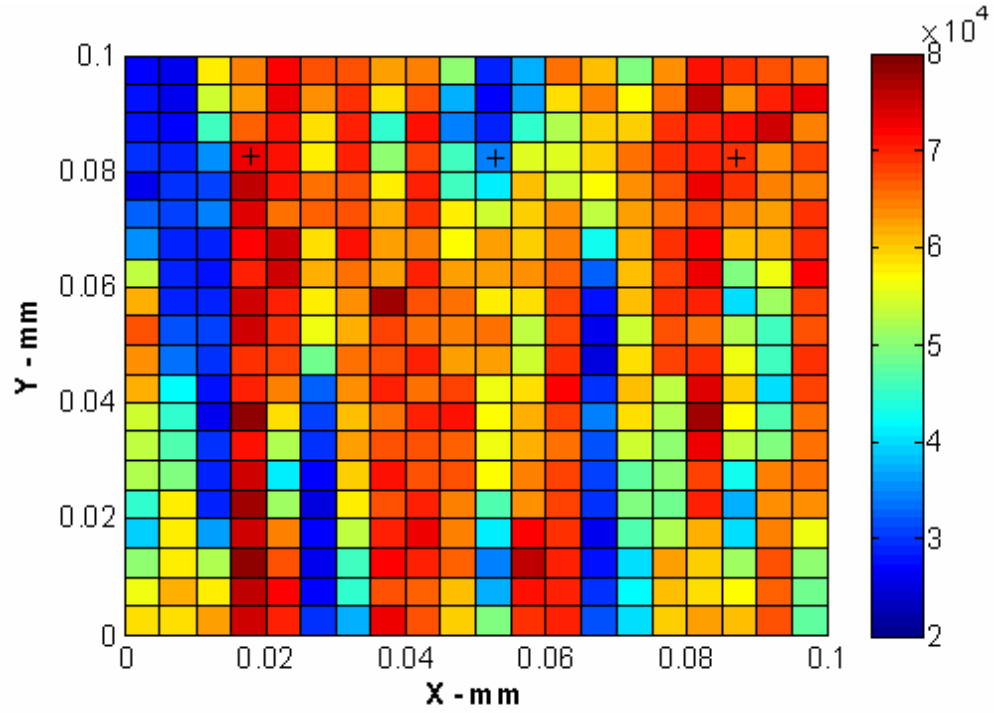

Fig. 72. Variation of the Q-factor for the Si-face (6 hrs.) annealed 40 min. under carbon dioxide flow.

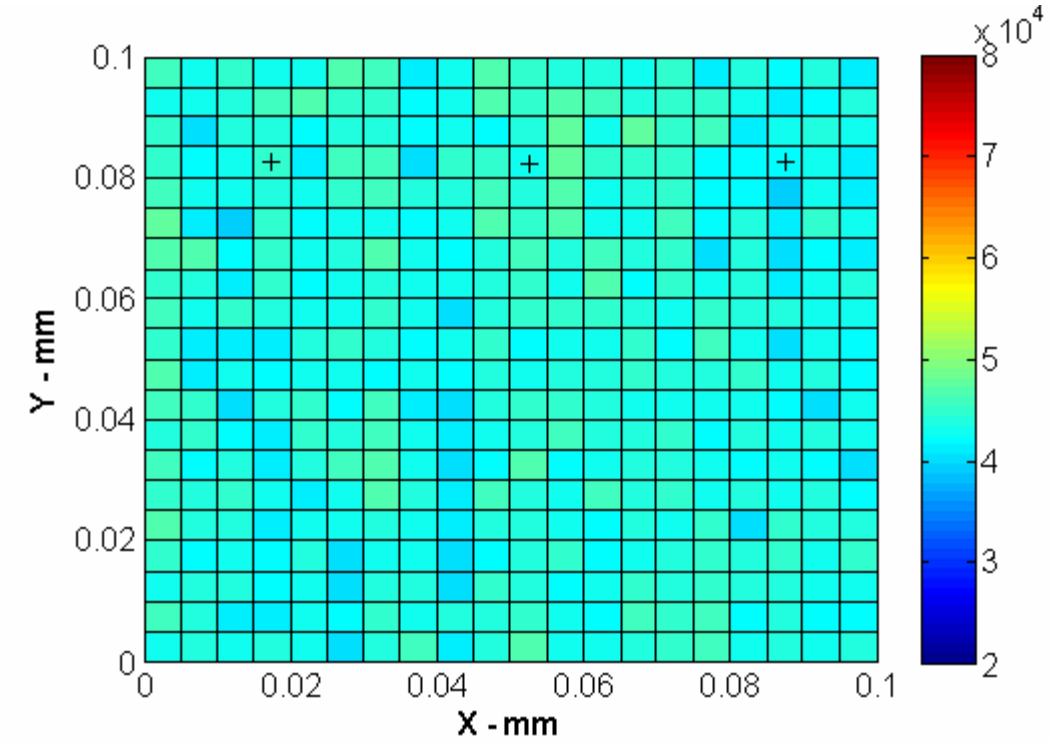

Fig. 73. Variation of the Q-factor for the Si-face (6 hrs.) annealed 60 min. under carbon dioxide flow.

The Q-factor for the Si-face (6 hrs.) was measured at the locations indicated by a "+" on the graphs before and after treatment. Table XV summarizes the values obtained at these three specific locations.

Table XV. Q-factor values at specific locations of Si-face(6 hrs.) CNT samples before and after treatment under carbon dioxide flow.

Coordinates	(4,17)	(11,17)	(18,17)
Q (untreated) (10^4 arb.units)	2.43	2.32	2.36
Q (treated 25 min.) (10^4 arb.units)	4.13	4.04	4.38
Q (treated 40 min.) (10^4 arb.units)	6.19	4.00	7.10
Q (treated 60 min.) (10^4 arb.units)	4.48	4.03	4.10

The mean Q-factor values for each case was calculated and the Q-factor values are summarized in Tab.XVI.

Tab.XVI. Mean Q-factor values for the untreated and treated Si-face (6 hrs.) CNT samples.

Sample	Mean Q-factor (10^4 arb.units)
Untreated Si-face (6 hrs.)	2.92
Treated Si-face (6 hrs.) for 25 min. under CO_2 flow	4.37
Treated Si-face (6 hrs.) for 40 min. under CO_2 flow	5.71
Treated Si-face (6 hrs.) for 60 min. under CO_2 flow	4.33

From the graphs (Fig. 70, Fig. 71, Fig. 72 and Fig. 73) and the values recorded in Table XV and Table XVII, the Q-factor of the Si-face (6 hrs.) sample improved by 50 % after annealing for 25 min. under oxygen flow. After annealing for 40 min., the Q-factor improves by total 95.5 % in reference to untreated CNT sample. The improvement in the Q-factor is due to partial uncapping and removal of the graphitic carbon layers and the adsorbed molecules at 25 min. and a complete uncapping at 40 min. However, after 60 min. of annealing in carbon dioxide atmosphere the Q-factor decreases by 24 % similar to annealing of CNT sample in oxygen atmosphere.

The multi-walled carbon nanotubes grow perpendicular to the surface of the substrate, with a larger diameter closer to the SiC substrate. After 25 min. of annealing, the caps of the CNT are partially removed together with the graphitic carbon and the adsorbed molecules such as oxygen. As a result of this annealing, a larger area of crystalline CNT film is exposed and local surface conductivity of the sample increases (Fig. 74(b)). After 40 min. of annealing, the CNT are uncapped completely and the surface area exposed for measurement of surface conductivity increases significantly (Fig. 74(c)). This could explain the increase in conductivity observed after 40 min. of treatement. However, after 60 min. of annealing, the CNT tubes are completely removed from the substrate leaving SiC behind with a lower conductivity than the CNT film (Fig. 74 (d)).

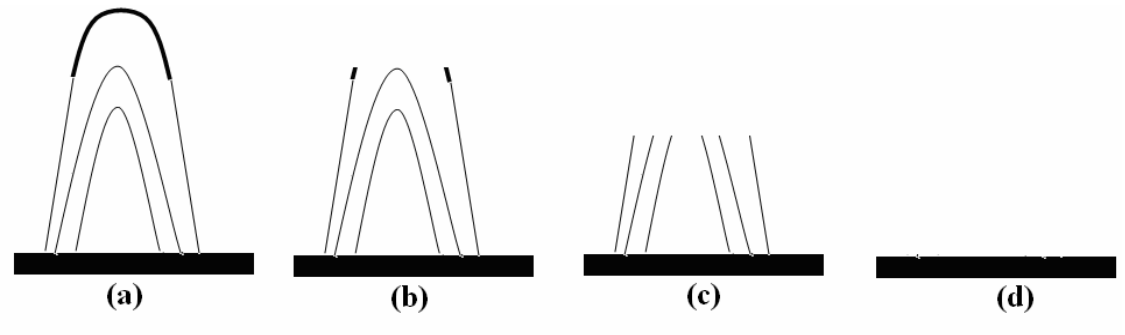

Fig. 74. Schematic diagram of untreated multi-walled CNT (a), partially uncapped CNT after 25 min. of annealing (b) uncapped CNT after 40 min. of annealing (c) and complete removal of the CNT from the substrate after 60 min. (d).

CHAPTER 8

CONCLUSION

The structural, chemical and electromagnetic characterizations of CNT films grown by the surface decomposition of silicon carbide have been studied . A theoretical model, based on the method of images, has been used to interpret the experimental data obtained from the evanescent microwave microscopy measurements of treated and untreated CNT films. The equations of the frequency shift of the resonator and the quality factor shift when the probe-tip touches the sample has also been derived and applied to the experimental measurements on the CNT films. The results from the theoretical model have also been compared to existing experimental data available in the literature.

I have reviewed the formation mechanism of CNT films. Carbon nanotube films can be grown in the absence of metal catalyst by the surface decomposition of silicon carbide. The quality of the CNT films is dependent on temperature and pressure. A thick layer of CNT film with a low percentage of amorphous carbon is formed at the pressure in the range from 10^{-3} Torr to 10^{-5} Torr and the temperature in the range of 1400^{o} C to 1700^{o} C . The growth mechanism of CNT films on the silicon and carbon terminated face of the silicon carbide substrate has been described. It was found that CNT films are formed on the carbon terminated face and parallel graphite sheets on the silicon face. However, if the silicon terminated face is cleaned and the silicon oxide layer removed from the surface, CNT can be obtained on the silicon face. As a result of this oxidation the length of the CNT on the Si-face is shorter than CNT grown on the C-face.

Structural characterization of the untreated CNT was performed by collaborators using SEM, TEM and AFM analyses. The cross-sectional SEM image shows that the CNT formed by the surface decomposition method are uniform vertically aligned, continuous and well-attached to the substrate. The CNT are single multi-walled and coalesced multi-walled, with varying height and diameters. The diameter of the CNT is larger closer to the substrate interface and smaller at the top. The top view SEM image shows the presence of whitish spots of graphitic carbon and adsorbed molecules such as oxygen which are attached to the surface when exposed to the air. This observation was

confirmed by the cross-sectional TEM image which shows a thin layer of amorphous carbon above the capped carbon nanotubes. The AFM image shows a dense agglomeration of the vertically aligned capped carbon nanotubes with different heights and diameters formed on the silicon carbide substrate. The top view TEM image also shows that multiple-walled and single multiple-walled CNT are coalesced, which explains the variation of the diameters of the carbon nanotubes from AFM image.

XRD and EDS measurements show that as the growth time of silicon carbide increases, the amount of silicon in the substrate decreases, demonstrating that silicon reacts preferentially with oxygen to form silicon oxide (Eq.(32)).

Evanescent microwave microscopy was used to characterize the CNT films subjected to annealing treatment at 400^{o} C under oxygen or carbon dioxide flow with a purpose to uncap them in order to increase conductive properties of these films. It was found that the surface conductivity increases after 25 min. of annealing under oxygen or carbon dioxide flow at 400^{o} C and the optimum conductivity was obtained after 40 min. of annealing under the same conditions. This conclusion was based on measured X-Y scans of the Q-factor (inversely proportional to the surface resistance) by evanescent microwave microscope. In order to have a better insight to these changes, SEM and AFM measurements were performed. It is clearly seen from AFM and SEM images that there is a partial uncapping of the CNT and a complete removal of the amorphous carbon layer after 25 min. of annealing and a complete uncapping of the CNT after 40 min. of annealing. This results in the largest area of the crystalline CNT presence after 40 min. of annealing on the surface of the film and better conductivity. However, after 60 min. of annealing, no significant features were observed on the surface, indicating the complete removal of the crystalline CNT film from the silicon carbide substrate, which lowers conductivity of the sample. This was confirmed by XRD pattern showing amorphous behavior of the sample.

The resonant frequency and reciprocal of the Q-factor shifts were also measured by evanescent microwave microscope. These data were fitted to our theoretical model and the real and imaginary component of complex permittivity of the CNT films before and after the annealing treatment were obtained. The real component of permittivity was 47 and 33.5 and the imaginary component was 13.5 and 15.0 for the untreated and treated

CNT films, respectively. An observed increase in the imaginary component of the permittivity from 13.5 to 15.0 indicates some improvement in conductivity for treated CNT. At the same time, a decrease in the real component of the permittivity from 47 to 33.5 suggests a decrease in the dielectric properties the treated CNT films.

The shift in frequency and in reciprocal of the Q-factor when the tip touches the samples was derived from theoretical model based on available experimental data. It was found that the shift in the resonant frequency is greater for the untreated CNT films and the shift in the reciprocal of the Q-factor is greater for the treated CNT films. It appears that the shift in the resonant frequency is proportional to the real part of permittivity ε' and that is why the untreated film has a greater value because of larger ε' in comparison to the shift for the treated film. The shift in the reciprocal of the Q-factor is proportional to ε'' and since the treated CNT have a greater ε'', they have a greater shift in the reciprocal of the Q-factor. In order to confirm the validity of the theoretical model, the resonant frequency shifts was checked for two dielectric materials, namely MgO and LAO and the results were compared with existing experimental data found in the literature. The frequency shifts calculated from the model confirmed these data.

FUTURE WORK

Field emission testing should be done on all CNT films subjected to our uncapping procedure to confirm our findings based on measurements of electromagnetic properties by using evanescent microwave microscopy.

REFERENCES

[1] M. O'Connell, "Carbon nanotubes: properties and applications", Boca Raton (Florida) CRC Taylor & Francis (2006).

[2] S. Sinnott and R. Andrews, " Carbon nanotubes: synthesis, properties, and applications", Crit. Rev. Solid State, **26**, 145 (2001).

[3] H. Dai, "Carbon nanotubes: synthesis, integration and properties", Acc. Chem. Res. **35**, 1035 (2002).

[4] S. Iijima, "Carbon nanotube and their recent developments", Proceedings of the IEEE, **98**, 520 (1998).

[5] H. Baltes, O. Brand, G.K. Fedder, C. Hierold, J.G. Korvink and O. Tabata, "Enabling technology for MEMS and nanodevices", Germany John Wiley-VCH (2004).

[6] R. Baughman, A. Zakhidov and W. Heer, "Carbon nanotubes - the route towards applications", Science, **297**, 787 (2002).

[7] University of Florida, Materials Science Page, http://www.mse.ufl.edu.

[8] R. Gomer, "Field emission and field ionization", Cambridge (Massachusetts) Harvard University Press (1961).

[9] G. Fursey, "Field emission in vacuum micro-electronics", Appl. Surf. Sci. **215**, 113 (2003).

[10] Z. Lin Wang and C. Hui, "Electron microscopy of nanotubes", Boston Kluwer Academic Publishers (2003).

[11] J.M. Bonard, H. Kind, T. Stockli and L. Nilsson, "Field emission from carbon nanotubes: the first five years", Solid State Electron. **45**, 893 (2001).

[12] R.G. Forbes, C.J. Edgcombe and U. Valdre, "Some comments on model for field enhancement", Ultramicros. **95**, 57 (2003).

[13] N. Jonge and J.M. Bonard, "Carbon nanotube electron sources and applications", Phil. Trans. R. Soc. Lond. **362**, 2239 (2004).

[14] M. Meyyappan, "Carbon nanotubes: science and applications", Boca Raton CRC Press (2005).

[15] G. Amaratunga, "Watching the nanotube", Spectrum IEEE, **40**, 28 (2003).

[16] J. Boeckl, W.C. Mitchel, J. Rigeur and W. Lu, "Structural and electrical characterization of carbon nanotubes formed on silicon carbide substrates by surface decomposition", Proc. Of Int'l Conf. on SiC and related mat'ls, 1579 (2005)

[17] M. Ito, S. Sago, T. Suzuki, M. Kusunoki, T. Hirayama and S. Uemura, "Field emission of carbon nanotube films formed by surface decomposition of SiC", International Display Manufacturers Conference, Korea (2002).

[18] K. Teo, "Carbon nanotube electron source technology", J. of mat. **59** (2007)

[19] R.A. Kleismit, M. ElAshry, G. Kozlowski, M. Amer, M.K. Kazimierczuk and R.R. Biggers, "Local dielectric and strain measurements in $YBa_2Cu_3O_{7-\delta}$ thin films by evanescent microscopy and Raman spectroscopy, Supercond. Sci. Technol. **18**, 1197 (2005).

[20] D.M. Pozar, "Microwave Engineering", Canada John Wiley & Sons, Inc. (1998).

[21] W.C Mitchel, J.Boeckl, D.Tomlin, W.Lu, J.Rigueur and J.Reynolds, "Growth of carbon nanotubes by sublimation of silicon carbide substrates", Quantum sensing and nanophotonic devices II, Proceedings of the SPIE, 5732, (2005).

[22] http://www.crpgl.lu/en/sam/sem.php3 (reference from internet).

[23] M. Kusunoki, T. Suzuki, K. Kaneko and M. Ito, "Formation of self-aligned CNT films by surface decomposition of silicon carbide", Phil. Mag. Lett. **79**, 153 (1999).

[24] M. Kusunoki, T. Suzuki, T. Hirayama and N. Shibata, "A formation mechanism of carbon nanotubes films on SiC(0001)", Appl. Phys. Lett. **77**, 531 (2000).

[25] T. Nagano, Y. Ishikawa and N. Shibata, "Effects of surface oxides of SiC on carbon nanotube formation by surface decomposition", Jpn. J. Appl. Phys. **42**, 1380 (2003).

[26] M. Kusunoki, T. Suzuki, T. Hirayama and N. Shibata, "Aligned carbon nanotube films on SiC (0001) wafers, Physica B, **323**, 296 (2002).

[27] H. Watanabe, Y. Hisada, S. Mukainakono and N. Tanaka, "In situ observation of the initial growth process of carbon nanotube by the time-resolved high resolution transmission electron microscopy", J. of Microsc. **203**, 40 (2001).

[28] J. Harrison, S. Sambandam, J. Boeckl, W.C. Mitchel, W.E. Collins and W. Lu, "Evaluation of metal-free carbon nanotubes formed by SiC thermal decomposition", J. Appl. Phys. **101**, (2007).

[29] C. Gao and X.D. Hiang, "Quantitative microwave near-field microscopy of dielectric properties", Rev. Sci. Instrum. **69**, 3846 (1998).

[30] C. Gao, B. Hu, I. Takeuchi, K.S. Chang, X.D. Xiang and G. Wang, "Quantitative scanning evanescent microwave microscopy and its applications in characterization of functional materials libraries", Meas. Sci. Technol.**16**, 248 (2005).

[31] C.A. Grimes, E.C. Dickey, D. Qian, C. Mungle and K.G. Ong, "Effect of purification on the electrical conductivity and complex permittivity of multiwall carbon nanotubes", J. Appl. Phys. **90**, 8879 (2001).

[32] J.A. Fagan, J.R. Simpson, B.J. Landi, L.J. Richter, I. M. Mandelbaum, V. Baijpai, D.L. Ho, R. Raffaelle, A.R. Hight Walker, B.J. Bauer and E.K. Hobbie, "Dielectric response of aligned semiconducting single-wall nanotubes", Phys.Rev.Lett. **89**, 147402 (2007).